https://doi.org/10.5194/egusphere-2026-4875
Preprint. Discussion started: 21 September 2026

Noah-MP-ML^2 v1.0: Development of a multilayer canopy land surface model with improved representation of vadose zone soil water dynamics

Harsh G. Kamath[1], Gordon B. Bonan[2], Zong-Liang Yang[1], Ronnie Abolafia-Rosenzweig[2], Cenlin He[2], Ashley Matheny[1], and Dev Niyogi[1]

[1]Department of Earth and Planetary Sciences, Jackson School of Geosciences, The University of Texas at Austin, Austin, TX, USA.
[2]NSF National Center for Atmospheric Research, Boulder, CO, USA.

Correspondence: Harsh G. Kamath (kamath.harsh@utexas.edu)

Abstract. Land surface models (LSMs) simulate the surface layer processes and land–atmosphere exchanges of energy, water, and carbon. However, many LSMs still rely on simplified surface layer radiation transfer, canopy turbulence, and vadose zone hydrology parameterizations. This paper describes the development of a multilayer canopy extension to the community Noah-MP LSM named Noah-MP-ML^2 to address these limitations. Noah-MP-ML^2 implements a roughness sublayer scheme and the Medlyn stomatal conductance parameterization to represent canopy turbulence and photosynthesis process. Further, the implementation of the Speedy Algorithm for Radiative Transfer through Cloud Sides (SPARTACUS) surface layer radiation transfer scheme enables consistent N-stream shortwave and longwave radiation transfer at multiple spectral bands. SPARTACUS also accounts for the lateral exchanges of radiation within the heterogeneous vegetation canopies. A multilayer canopy implicit solution is used to calculate the canopy scalars and leaf temperature of sunlit and shaded foliage. To calculate soil water diffusion and update soil liquid water, we implemented a mixed form of mass-conserving 1-D Richards equation solver that uses the van Genuchten water retention curves. Noah-MP-ML^2 was evaluated against observations at five flux tower sites that span different forest types and diverse background climate regimes. Results demonstrated improved representation of surface layer energy partitioning, turbulence (friction velocity), and soil water dynamics relative to the community Noah-MP LSM.

1 Introduction

Land surface models (LSMs) partition the available energy at the surface layer into heat fluxes and convert available water into evapotranspiration flux, storage, and runoff (Pitman, 2003). The turbulent heat fluxes produced by LSMs serve as boundary conditions to the atmospheric models, which use them to simulate phenomena ranging from sub-daily weather patterns to long-term climate trends and variability. Additionally, since the land surface acts as carbon sources/sinks, LSMs simulate the carbon cycle. The first generation of LSMs solved a simple energy balance without accounting for soil heat flux and employed a rudimentary "bucket" model for hydrology (Manabe, 1969). The second generation of LSMs introduced a layered soil structure and distinguished between soil and vegetation layers (Deardorff, 1978). For the vegetation layer, a dual-source canopy

https://doi.org/10.5194/egusphere-2026-4875
Preprint. Discussion started: 21 September 2026

model was used, where the aerodynamic resistance terms were calculated using micrometeorological methods. The stomatal conductance derived from the Jarvis model (Jarvis, 1976) was combined with leaf boundary layer resistance to estimate water vapor flux. As a result, the second-generation LSMs significantly improved the representation of energy and hydrological processes (Dickinson et al., 1986; Sellers et al., 1986). The third generation of LSMs further advanced by calculating stomatal conductance based on photosynthetic processes (Ball et al., 1987; Farquhar et al., 1980), enabling explicit simulation of the water-energy-carbon cycle.

A shortcoming with the second- and third-generation dual-source canopy models is that they do not explicitly resolve the vertical structure of the canopy. The ability to resolve the canopy structure is important in LSMs because leaf area is vertically distributed in a heterogeneous way and must be accounted for to accurately represent canopy processes, such as stomatal conductance. For instance, the stomatal conductance for the upper leaves may be higher due to the abundance of radiation, which attenuates exponentially based on the leaf area availability as it travels within the canopy. To account for such effects, multilayer canopy models were proposed in the late 1960s (Waggoner and Reifsnyder, 1968), followed by more comprehensive formulations incorporating coupled radiative transfer, leaf energy balance, and photosynthesis (Baldocchi and Harley, 1995; Goudriaan, 1977; Norman, 1979). However, these multilayer models were rarely coupled with atmospheric models, as they required iterative solutions for stomatal conductance, leaf temperature, and radiation for each of the leaf layers within the canopy and the canopy as a whole and hence were computationally prohibitive for coupled simulations. Recent developments in implicit numerical schemes for canopy processes (Ryder et al., 2016) has revived interest in multilayer canopy models within the LSM community (Bonan et al., 2018). Additionally, the following gaps in surface-layer process representation in the community Noah-MP LSM have motivated the development of the multilayer canopy model (Noah-MP-ML^2) discussed in this paper:

1.1 Canopy-atmosphere exchange coefficient

The community Noah-MP LSM (He et al., 2023b; Niu et al., 2011; Yang et al., 2011) follows the dual-source canopy configuration for aerodynamic resistance calculation and relies on the Monin–Obukhov similarity theory (MOST) to represent turbulent exchanges between vegetation canopy and the atmosphere. However, the flux-gradient relationships predicted by MOST are only applicable in the inertial sub-layer or the constant flux layer. Measurements above tall forest canopies in the roughness sub-layer (RSL), which typically extends up to 2-3 times the canopy height, have shown systematic departures from MOST (Garratt, 1980). Within the RSL, the diffusivities for momentum and scalars can exceed the MOST prediction by more than a factor of two (Raupach and Thom, 1981). These departures arise since MOST assumes that the characteristic length scale of eddies within the canopy reduces with height, but the characteristic length scales are proportional to the canopy height rather than the distance from the surface in the RSL (Kaimal and Finnigan, 1994).

1.2 Canopy radiation transfer

The community Noah-MP LSM does not account for the lateral exchanges of radiation between vegetated and bare regions within the canopy space and the 3-D structure of the canopy and gaps within the canopies are accounted for using a gap proba-

https://doi.org/10.5194/egusphere-2026-4875
Preprint. Discussion started: 21 September 2026

bility approach (Niu and Yang, 2004) that modifies the 2-stream approximation for horizontally homogeneous canopies in the shortwave band (Dickinson, 1983; Sellers, 1985). The longwave radiation transfer in the community Noah-MP is inconsistent with the 2-stream model in shortwave, where a bulk emissivity and temperature-based formulation is used to calculate the longwave fluxes, and then the fluxes are aggregated at the grid cell level using fractional vegetation coverage.

1.3 Photosynthetic and hydrological processes

The community Noah-MP model implements the Ball–Berry stomatal conductance model (Ball et al., 1987) with Farquhar type photosynthesis model (Farquhar et al., 1980). The Ball-Berry model uses a linear relationship to relate stomatal opening to leaf surface relative humidity. However, models based on water use efficiency show that this relation is not linear (Bonan et al., 2014; Franks et al., 2017; Medlyn et al., 2011). Finally, the soil water diffusion in Noah-MP is simulated by solving a mass-conserving moisture-form of the Richards equation (Richards, 1931) that was inherited from the original Noah LSM (Chen and Dudhia, 2001; Ek et al., 2003). In this solver, the infiltration is provided as a flux boundary condition at the surface. However, there are known shortcomings of this solver, including temporary supersaturation within layers, redistribution of soil liquid water through adjustments and water balance concerns (He et al., 2023b, c).

To address these gaps, we build upon the multilayer canopy implicit solution and the Harman-Finnigan RSL scheme (Harman and Finnigan, 2007, 2008) implementation by Bonan et al. (2018) to develop Noah-MP-ML^2. Additionally, we implemented the Medlyn stomatal conductance model (Medlyn et al., 2011) within the community Noah-MP and Noah-MP-ML^2. The Speedy Algorithm for Radiative Transfer through Cloud Sides (SPARTACUS) is implemented as the multilayer canopy radiative transfer scheme, enabling a consistent 2N-stream radiation solution with lateral radiative exchanges for heterogeneous vegetation canopies in both shortwave and longwave bands (Hogan, 2019; Hogan et al., 2018). Because soil moisture availability directly regulates stomatal conductance and transpiration, vadose zone soil water dynamics must be correctly represented in LSMs. Thus, a mass-conserving mixed-form of the Richards equation with adaptive time stepping that uses the van Genuchten soil water retention curves (van Genuchten, 1980) was also implemented. The Richards equation is solved on a 20-layer stretched soil grid to avoid the solver convergence issues under strong wetting fronts and to calculate the infiltration. All developments are implemented within the Noah-MP version 5 framework (He et al., 2023b). Noah-MP-ML^2 therefore represents a continued model-development effort within the Noah-MP version 5+ framework, with selected canopy and subsurface processes adapted from the community Noah-MP and CLM-ml v0 (Bonan et al., 2018) models, while the modifications and newly implemented processes are described in this paper. Figure 1a compares Noah-MP and Noah-MP-ML^2, highlighting the enhanced representation of canopy radiation, turbulence, stomatal conductance and soil hydrology. Figure 1b illustrates how these process-level improvements lead to improvements in the simulated fluxes and states.

https://doi.org/10.5194/egusphere-2026-4875
Preprint. Discussion started: 21 September 2026

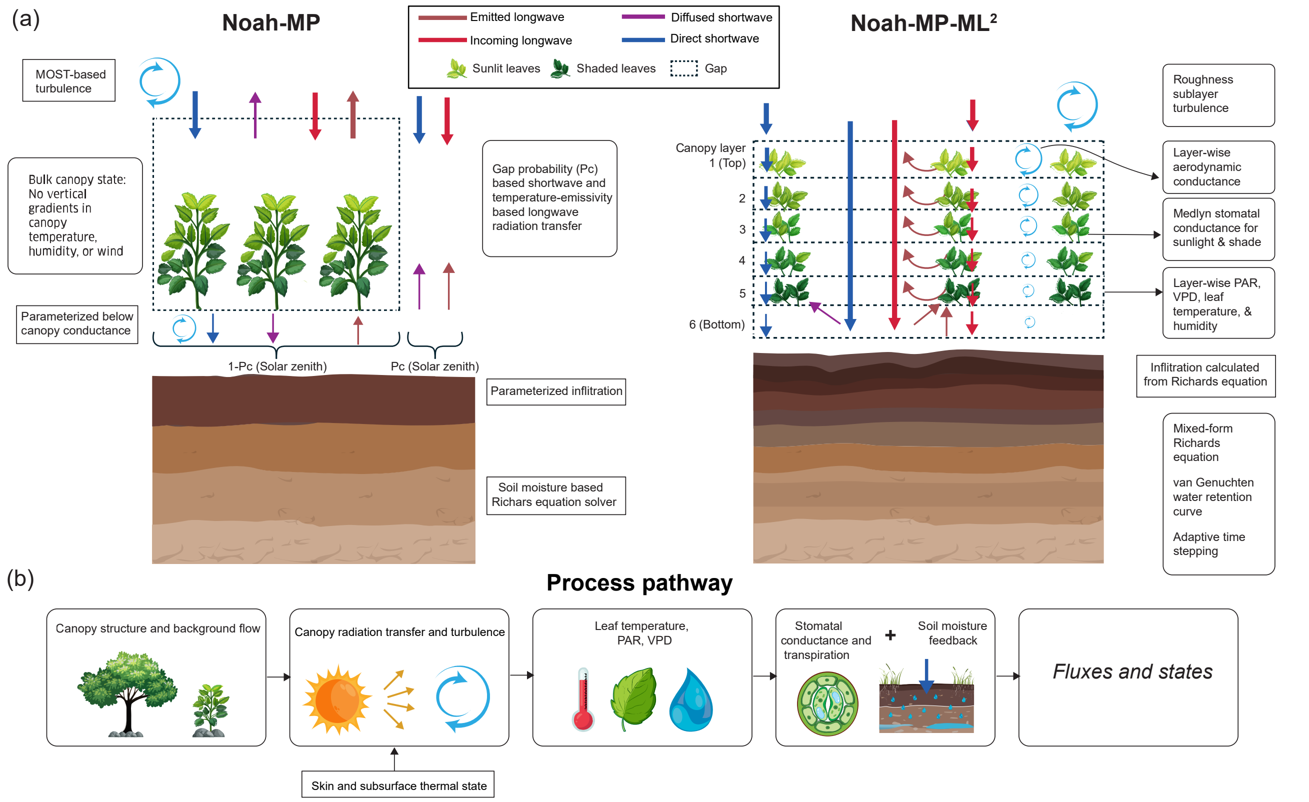

Figure 1. (a) Simplified representation comparing the community Noah-MP model with Noah-MP-ML^2: canopy radiation transfer, turbulence, transpiration and soil hydrology processes are shown. (b) Illustration of the pathway by which the process-level improvements in Noah-MP-ML^2 result in improved land fluxes and states.

2 Noah-MP-ML^2 model overview

Compared to the community Noah-MP, Noah-MP-ML^2 supports sub-grid tiling within each model grid cell to represent spatial heterogeneity in land cover, as shown in Figure 2a. Each landcover tile can be associated with its own canopy structure and soil column, while all sub-grid tiles are driven by the same atmospheric forcing. Grid mean fluxes are aggregated across the tiles using the fraction of area covered by the individual tiles.

Within each vegetated tile, fractional vegetation coverage (c_{veg}) can be prescribed or diagnosed using the effective leaf area index (LAI), which is zero for non-vegetated tiles. Radiative transfer for the vegetated tile is computed considering gaps in vegetation, quantified by c_{veg} and vegetation horizontal scale, while the heat fluxes are computed separately for vegetated and bare ground fractions and are subsequently aggregated using c_{veg} to obtain tile-mean fluxes as shown in Figure 2b. Canopy water interception, evaporation, and throughfall are also calculated in the vegetated tile based on c_{veg}.

https://doi.org/10.5194/egusphere-2026-4875
Preprint. Discussion started: 21 September 2026

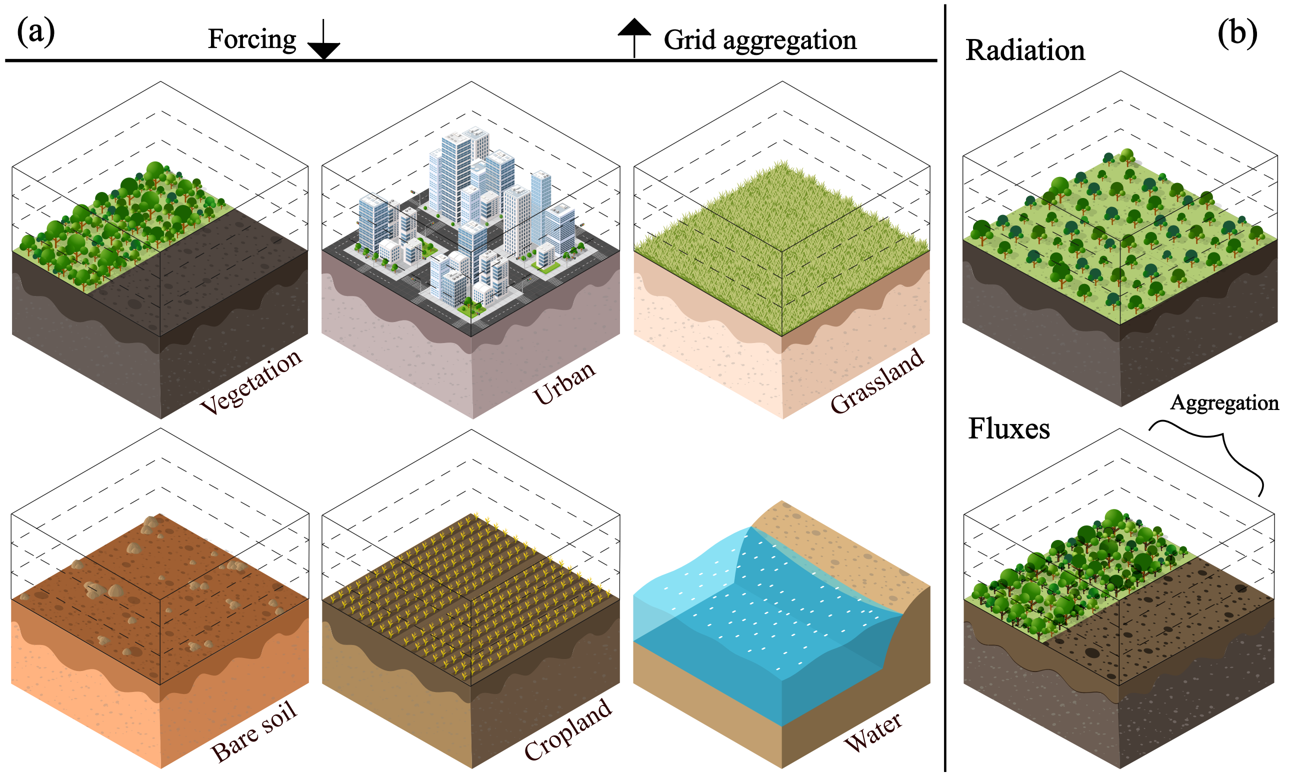

Figure 2. (a) Illustration of the sub-grid tiling concept. Representative land cover types are shown as sub-grid tiles. (b) Calculation of radiation transfer and fluxes for the vegetated tile.

3 Enhanced multilayer canopy processes in Noah-MP-ML^2

In the multilayer canopy configuration, the canopy and the air column up to the forcing height are discretized as shown in Figure 3. The canopy is divided into uniform layers by prescribing the forcing and canopy heights along with the target vertical resolution of the grid. The canopy scalars are defined at layer midpoints, and leaf area is distributed following a beta distribution that ensures the conservation of total LAI (Bonan et al., 2018). The parameters of the beta distribution are based on the shape of the canopy. Each layer has its own wind speed, specific humidity, leaf temperature, and air temperature. Note that the model distinguishes between sunlit and shaded foliage. There is aerodynamic conductance (g_i) between adjacent scalars θ_i and $\theta_{i+1)}$. The example shown in Figure 3 is for sensible heat flux where there is a leaf boundary layer resistance (g_{bh}) between the leaf and air. The calculation of boundary layer resistance for heat, water vapor and carbon in Noah-MP-ML^2 follow Monteith and Unsworth (2013). The heat flux due to the gradient between surface temperature (T_{ground}) and air temperature of the first model layer is bottom boundary condition, while the atmospheric forcing is the top boundary condition.

https://doi.org/10.5194/egusphere-2026-4875
Preprint. Discussion started: 21 September 2026

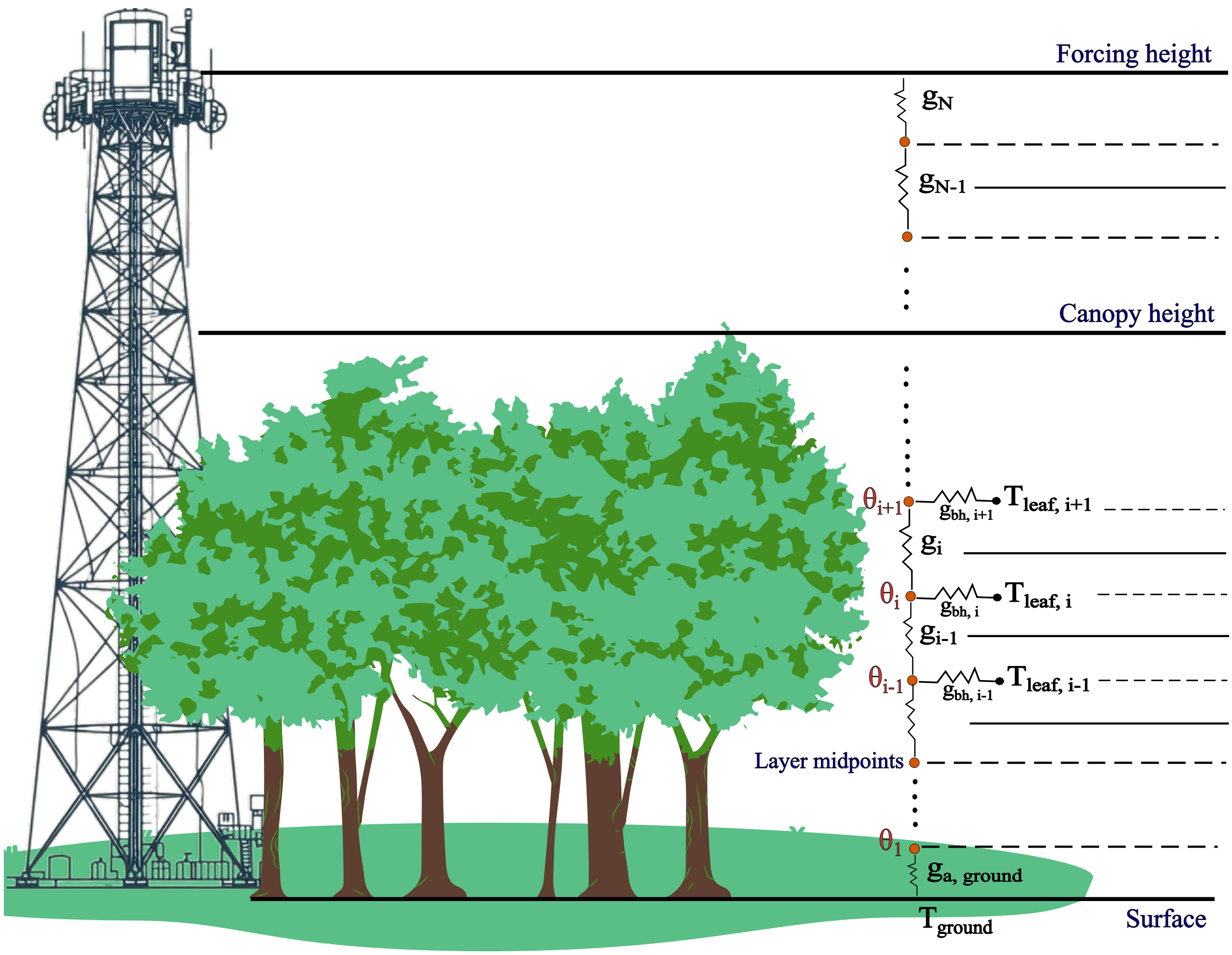

Figure 3. Illustration of canopy set-up for the vegetated (sensible heat flux example).

3.1 Stomatal conductance

The Medlyn stomatal conductance model was implemented in both community Noah-MP and Noah-MP-ML[2]. The community Noah-MP implementation of the Medlyn model follows the framework similar to the existing Ball-Berry model, while the Medlyn implementation in the multilayer configuration follows a more detailed implementation similar to Bonan et al. (2018).

3.1.1 Implementation of the Medlyn scheme in the community Noah-MP

The community Noah-MP model currently uses the Ball–Berry model to link photosynthesis and stomatal conductance for sunlit and shaded foliage under C_3 and C_4 photosynthetic pathways. The formulations for Rubisco- and light-limited photosynthesis, as well as the minimum-conductance and slope parameters, differ between the C_3 and C_4 pathways. In the Ball–Berry

https://doi.org/10.5194/egusphere-2026-4875
Preprint. Discussion started: 21 September 2026

model, the stomatal conductance for water vapor (g^{sw}, $\mathrm{mol\,m^{-2}\,s^{-1}}$) declines linearly with relative humidity at the leaf surface (Ball et al., 1987), whereas the Medlyn model predicts a weaker, inverse-square-root dependence of g^{sw} on vapour pressure deficit (VPD) (Medlyn et al., 2011).

Building on the existing Farquhar-type photosynthesis formulation in the community Noah-MP, we implemented the Medlyn stomatal conductance model. For sunlit and shaded foliage, leaf photosynthesis is computed using Rubisco-, light-, and export-limited rates. The model uses Michaelis–Menten kinetics for CO_2 and O_2. The nitrogen-scaling and soil-moisture-stress factors (β_{soil}) are applied to the maximum carboxylation rate ($V_{c,\max}$). The CO_2 concentration at the leaf surface (c_s, $\mathrm{\mu mol\,mol^{-1}}$) is calculated using the ambient CO_2 concentration and the boundary-layer conductance to CO_2 (g^{bc}, $\mathrm{mol\,m^{-2}\,s^{-1}}$). The intercellular CO_2 concentration (c_i, Pa) and gross CO_2 assimilation (A_g, $\mathrm{\mu mol\,m^{-2}\,s^{-1}}$) are calculated iteratively using three iterations. The initial guess differs between the C_3 and C_4 pathways and is 0.7 and 0.4 times the ambient CO_2 concentration, respectively. Note that the community Noah-MP does not subtract leaf respiration from carbon assimilated during the calculation of stomatal conductance; thus, A_g is used. However, the leaf-respiration term is included when calculating the carbon budget. The Medlyn stomatal conductance is given by

$$g^{sw} = g_0^{sw} + D_{\mathrm{HC}} \cdot \left(1 + \frac{g_1^{sw}}{\sqrt{\mathrm{VPD}}}\right) \cdot \frac{A_g}{c_s}, \tag{1}$$

where g_0^{sw} is the minimum Medlyn stomatal conductance ($\mathrm{mol\,m^{-2}\,s^{-1}}$), g_1^{sw} is the Medlyn slope parameter ($\mathrm{kPa^{1/2}}$), and D_{HC} is the ratio of the diffusivity of H_2O to that of CO_2. A minimum value is imposed on g^{sw} for numerical stability. The conductance g^{sw} is then converted to the stomatal conductance for CO_2 (g^{sc}, $\mathrm{mol\,m^{-2}\,s^{-1}}$) and is subsequently used to update c_i according to the demand–supply balance.

3.1.2 Implementation of the Medlyn scheme in Noah-MP-ML^2

In the multilayer canopy, the stomatal conductance is solved layer-wise for sunlit and shaded leaves individually. The biochemical parameters at 25 °C for sunlit and shaded foliage are distributed vertically using an exponential leaf nitrogen profile. For both C_3 and C_4 pathways, the temperature dependent Michaelis–Menten constants for CO_2 and O_2, CO_2 compensation point, $V_{c,\max}$, electron transport rate, and leaf respiration rate are updated using Arrhenius and high temperature inhibition functions. Soil moisture stress or β_{soil} is applied to $V_{c,\max}$.

For each layer, the intercellular CO_2 (here $\mathrm{\mu mol\,mol^{-1}}$) and net CO_2 assimilation (A_n) are then solved iteratively using the Farquhar photosynthesis model with pathway dependent initial guesses of c_i as mentioned previously. Within each iteration, c_s is diagnosed from A_n and g^{bc}. Using A_n, c_s and VPD at the leaf, g^{sw} is computed. The resulting g^{sw} is converted to g^{sc} and is combined in series with g^{bc} to give the total leaf CO_2 conductance, which is then used to update c_i. The iteration is repeated until the diffusive constraints on CO_2 converge, yielding the final value of g^{sw}.

Figure 4 shows the behavior of g^{sw} following the Medlyn and Ball-Berry stomatal conductance models implemented within the community Noah-MP. Figure 4a highlights the Ball–Berry linear dependence on relative humidity; at fixed leaf temperature, this translates into an approximately linear relationship when plotted against VPD. Note that for a given VPD, the Medlyn

https://doi.org/10.5194/egusphere-2026-4875
Preprint. Discussion started: 21 September 2026

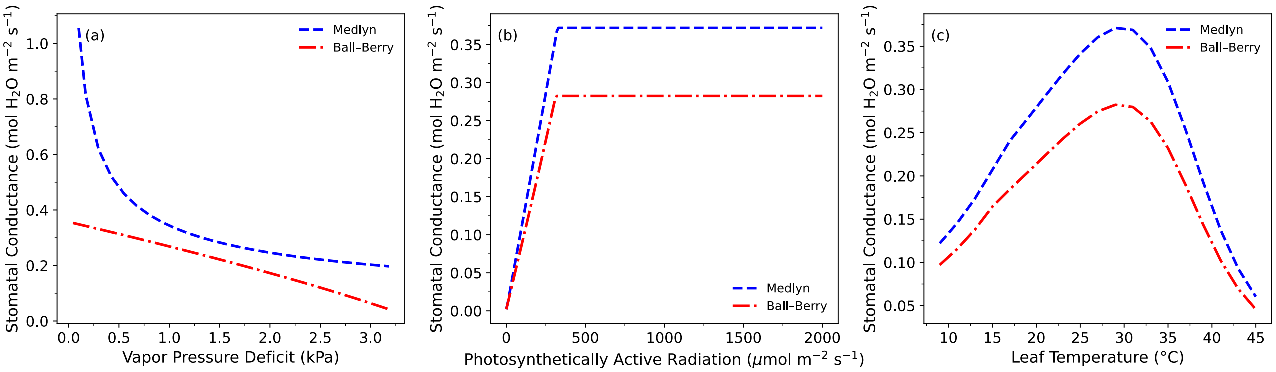

Figure 4. Stomatal conductance simulation for a representative deciduous broadleaf plant using the Medlyn and Ball–Berry models. Ball-Berry parameters: $g_0 = 0.002\,\mathrm{mol\,m^{-2}\,s^{-1}}$ and $g_1 = 9$. Medlyn parameters: $g_0 = 0.0001\,\mathrm{mol\,m^{-2}\,s^{-1}}$ and $g_1 = 4.45\,\mathrm{kPa}^{1/2}$. Photosynthesis follows the Noah-MP biochemical scheme with $V_{c,\mathrm{max}25} = 60\,\mathrm{\mu mol\,m^{-2}\,s^{-1}}$ and a leaf boundary layer resistance of $18.3\,\mathrm{s\,m^{-1}}$. Baseline conditions are Photosynthetically active radiation (PAR) $= 2000\,\mathrm{\mu mol\,m^{-2}\,s^{-1}}$, $CO_2 = 380\,\mathrm{\mu mol\,mol^{-1}}$, pressure $= 101325\,\mathrm{Pa}$, and leaf temperature $= 30\,^\circ\mathrm{C}$. (a) Stomatal conductance as a function of vapor pressure deficit (VPD), generated by varying relative humidity from 20 to 99 % at constant leaf temperature. (b) Stomatal conductance as a function of PAR, which is varied from 0–$2000\,\mathrm{\mu mol\,m^{-2}\,s^{-1}}$. (c) Stomatal conductance as a function of leaf temperature, which is varied from 9 to $45\,^\circ\mathrm{C}$. For Ball-Berry, relative humidity is fixed at 0.80 (VPD changes with temperature) and for Medlyn, VPD is held constant at $0.85\,\mathrm{kPa}$ by varying the relative humidity. Figure style adopted from Franks et al. (2017).

model predicts a higher g^{sw} (Figure 4a). Thus, with the slope parameter used, g^{sw} is higher for the Medlyn model when swept through the photosynthetically active radiation (PAR) and leaf temperature (Figures 4b and 4c). Note that when comparable Ball-Berry and Medlyn slope parameters were used, the PAR and leaf temperature responses were similar between the two model in the study by Franks et al. (2017).

3.2 Canopy radiation transfer

SPARTACUS is a 2N-stream radiation transfer model in both shortwave and longwave bands that uses an efficient matrix-based solver to obtain radiative fluxes in the surface layer (Hogan et al., 2018; Hogan, 2019). The N discrete angles at which the diffuse radiation travels in each of the hemispheres and the associated weights are calculated using double Gauss quadrature. The scheme accounts for lateral exchanges of radiation between clear and vegetated regions, thus enabling statistical representation of 3-D canopy effects. The SPARTACUS solver also allows for efficient simultaneous radiation transfer solution in k spectral bands in shortwave and l spectral bands in longwave. This multiband capability not only allows coupling with photosynthesis models but will also facilitate coupling with fluorescence models in the future. The scheme allows for the representation of two or three permeable regions (clear air and a maximum of two vegetated regions with different extinction coefficients). The longwave radiation transfer calculation in SPARTACUS is similar to the diffuse shortwave radiation but replaces the direct radiation scattering source with thermal radiation emission due to the foliage temperature.

https://doi.org/10.5194/egusphere-2026-4875
Preprint. Discussion started: 21 September 2026

Noah-MP-ML^2 uses different volumetric extinction coefficients for direct and diffuse radiation at each spectral band. These are calculated using the Ross-Goudriaan leaf projection function (G_{dif}) (Ross, 1975, 1981). For the i^{th} layer, extinction coefficient for diffuse radiation ($\mathrm{Ext}_i^{\mathrm{dif}}$) is

$$\mathrm{Ext}_i^{\mathrm{dif}} = \frac{G_{\mathrm{dif}}\,\mathrm{LAI}_i}{dz_i}, \tag{2}$$

where LAI_i is the layer-wise leaf area index ($\mathrm{m^2\,m^{-2}}$) and dz_i is the thickness of the layer (m). The diffuse projection function is calculated from the leaf angle departure parameter (χ_l) (Goudriaan, 1977; Ross, 1981) as

$$\phi_1 = 0.5 - 0.633\chi_l - 0.33\chi_l^2, \tag{3}$$

$$\phi_2 = 0.877\,(1 - 2\phi_1)\,, \tag{4}$$

$$G_{\mathrm{dif}} = \phi_1 + \frac{2\phi_2}{3}. \tag{5}$$

The value of χ_l depends on the vegetation type and describes the departure of the leaf angle distribution from the spherical distribution. The extinction coefficient for direct radiation is computed similarly using the direct beam Ross–Goudriaan function (G_{dir}):

$$G_{\mathrm{dir}}\,(\Theta_z) = \phi_1 + \phi_2 \cos\Theta_z, \tag{6}$$

$$\mathrm{Ext}_i^{\mathrm{dir}} = \frac{G_{\mathrm{dir}}\,(\Theta_z)\,\mathrm{LAI}_i}{dz_i}, \tag{7}$$

where Θ_z is the solar zenith angle. Note that in our formulation, G_{dir} is not divided by $\cos\Theta_z$ because SPARTACUS applies this scaling internally while constructing the direct beam extinction terms. For longwave radiation, Noah-MP-ML^2 uses the same extinction coefficient as for the diffuse shortwave radiation.

3.2.1 Shortwave absorption by foliage

Given the incident shortwave direct (S_k^{dir}) and diffuse (S_k^{dif}) shortwave radiations (in $\mathrm{W\,m^{-2}}$) at the top of canopy in spectral band (or wavelength) k, for each canopy layer i, SPARTACUS solves the radiation transfer for a unit direct beam and a unit diffuse shortwave radiation to obtain: (i) total vegetation absorption (direct + diffuse) per unit incident flux ($A_{i,k}^{\mathrm{tot}}$), (ii) absorption only due to the direct beam ($A_{i,k}^{\mathrm{dir}}$), (iii) absorption only due to diffuse ($A_{i,k}^{\mathrm{dif}}$), and (iv) sunlit fraction (f_i^{sun}).

https://doi.org/10.5194/egusphere-2026-4875
Preprint. Discussion started: 21 September 2026

The layer integrated shortwave absorption per unit ground area at i^{th} layer for sunlit ($Q_{i,k}^{\text{sun}}$) and shaded ($Q_{i,k}^{\text{sha}}$) foliage in $\mathrm{W\,m^{-2}}$ is given by

$$Q_{i,k}^{\text{sun}} = S_k^{\text{dir}} \cdot A_{i,k}^{\text{dir}} + f_i^{\text{sun}} \left[S_k^{\text{dif}} \cdot A_{i,k}^{\text{dif}} + S_k^{\text{dir}} \cdot \left(A_{i,k}^{\text{tot}} - A_{i,k}^{\text{dir}} \right) \right], \tag{8}$$

$$Q_{i,k}^{\text{sha}} = \left(1 - f_i^{\text{sun}}\right) \left[S_k^{\text{dir}} \cdot \left(A_{i,k}^{\text{tot}} - A_{i,k}^{\text{dir}} \right) + S_k^{\text{dif}} \cdot A_{i,k}^{\text{dif}} \right]. \tag{9}$$

The sunlit foliage receives both direct and diffuse radiations, while the shaded foliage only receives the diffuse radiation. The absorbed shortwave radiation per unit leaf area (in $\mathrm{W\,m^{-2}}$) for sunlit ($q_{i,k}^{\text{sun,SW}}$) and shaded ($q_{i,k}^{\text{sha,SW}}$) foliage is

$$q_{i,k}^{\text{sun,SW}} = \frac{Q_{i,k}^{\text{sun}}}{f_i^{\text{sun}} \cdot \mathrm{LAI}_i}, \tag{10}$$

$$q_{i,k}^{\text{sha,SW}} = \frac{Q_{i,k}^{\text{sha}}}{\left(1 - f_i^{\text{sun}}\right) \cdot \mathrm{LAI}_i}. \tag{11}$$

Figure 5 shows the canopy transmitted, absorbed, and reflected fluxes as a function of Θ_z for a unit direct beam radiation forcing at the top of the canopy in the visible band. Results are shown for the SPARTACUS model and gap probability-based 2-stream model currently available in the community Noah-MP. The simulations were conducted for low and high surface albedos (α_{s}), which are representative of bare soil and snow surfaces, and for open and dense forest structure defined by fractional vegetation coverage c_{veg} (Hogan et al., 2018). Figure 5 shows the SPARTACUS results for two-region/2-stream and three-regions/4-stream model configurations. SPARTACUS three-regions/4-stream model is considered as a benchmark as it performed the best when compared with the Monte Carlo simulations by Widlowski et al. (2011) at different Θ_z (Hogan et al., 2018). Across cases, increasing Θ_z reduces transmission while increasing the canopy absorption, with stronger sensitivity under a high albedo surface. Compared to SPARTACUS, Noah-MP shows the largest differences for sparse canopies over bright surfaces, highlighting the important role of lateral radiative exchange in the SPARTACUS model.

3.2.2 Longwave emission and absorption by foliage

The SPARTACUS longwave model solves for radiative fluxes due to the internal thermal emission and for a unit downwelling longwave radiation boundary condition at the canopy top. Given an incident longwave downwelling radiation (in $\mathrm{W\,m^{-2}}$) from sky in spectral band l (L_l^{sky}), for the canopy layer i, SPARTCUS provides the net longwave absorbed per unit ground area by vegetation in each layer, accounting for both absorption of radiation originating from adjacent regions and the vegetation's own thermal emission ($R_{i,l}^{\text{emit}}$), and foliage absorption from the unit downwelling longwave forcing ($R_{i,l}^{\text{abs}}$). The per unit leaf area longwave fluxes for the i^{th} layer are

https://doi.org/10.5194/egusphere-2026-4875
Preprint. Discussion started: 21 September 2026

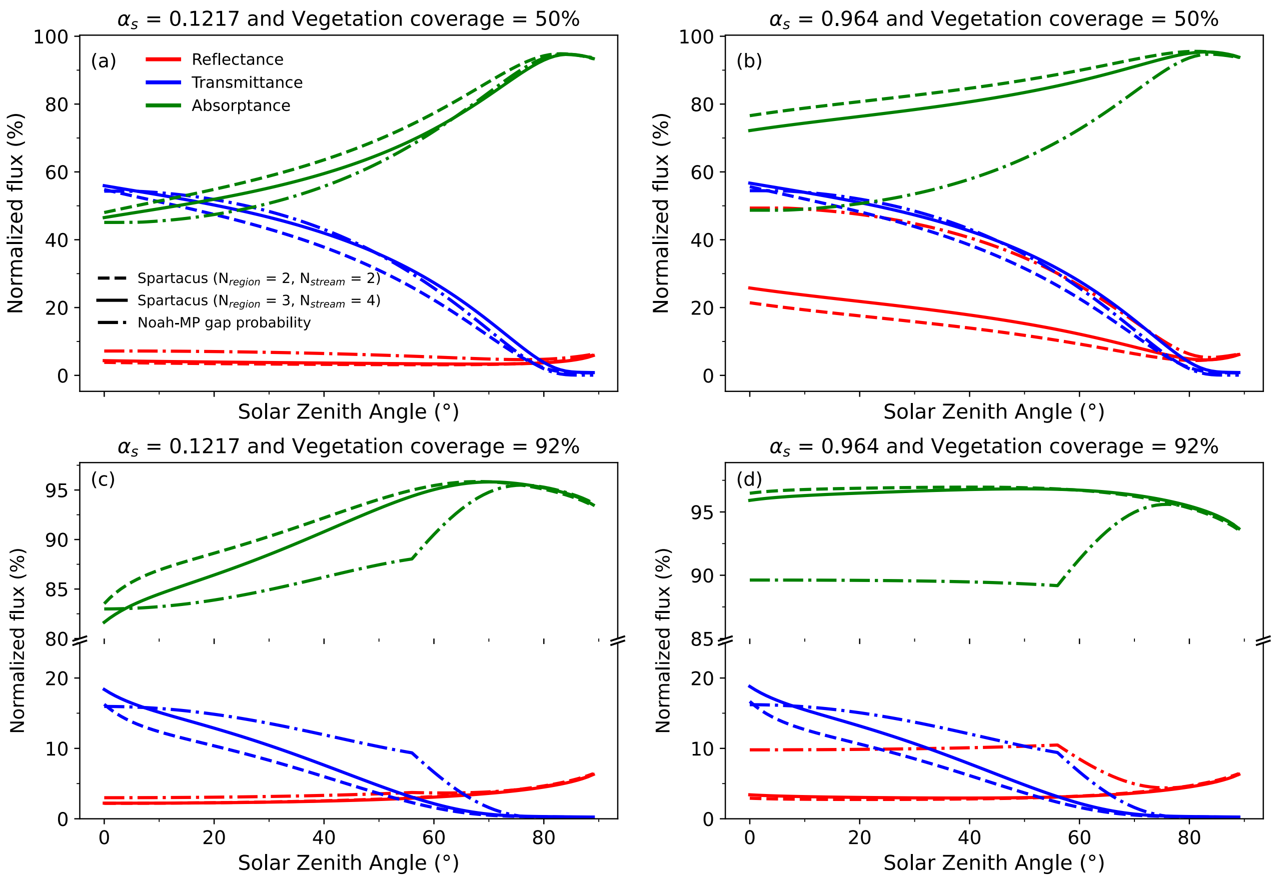

Figure 5. Reflected, absorbed, and transmitted radiation flux simulation for a unit direct beam radiation forcing at the top in the visible band. Parameters: leaf area index $= 5\,\mathrm{m}^2\,\mathrm{m}^{-2}$, leaf reflectance $= 0.0735$, leaf transmittance $= 0.0566$, spherical leaf angle distribution, canopy radius $= 5\,\mathrm{m}$, foliage top $= 14\,\mathrm{m}$, foliage bottom $= 4\,\mathrm{m}$. Results for SPARTACUS model under two configurations are shown: (i) 2-regions/2-stream model and (ii) 3-region/4-stream model. The gap probability model in Noah-MP was employed. (a) representative sparse forest with soil surface ($\alpha_s = 0.1217$ and $c_{\mathrm{veg}} = 0.5$). (b) representative sparse forest with snow surface ($\alpha_s = 0.964$ and $c_{\mathrm{veg}} = 0.5$). (c) representative dense forest with soil surface ($\alpha_s = 0.1217$ and $c_{\mathrm{veg}} = 0.92$) and (d) representative dense forest with snow surface ($\alpha_s = 0.964$ and $c_{\mathrm{veg}} = 0.92$). Note that the y-axis scale in the bottom panels (dense canopy) is different from the top panels (sparse canopy).

$$q_{i,l}^{\mathrm{emit,LW}} = \frac{R_{i,l}^{\mathrm{emit}}}{\mathrm{LAI}_i}, \tag{12}$$

$$q_{i,l}^{\mathrm{abs,LW}} = \frac{L_l^{\mathrm{sky}} \cdot R_{i,l}^{\mathrm{abs}}}{\mathrm{LAI}_i}. \tag{13}$$

In our implementation, the longwave radiation is assumed to be the same for sunlit and shaded foliage.

https://doi.org/10.5194/egusphere-2026-4875
Preprint. Discussion started: 21 September 2026

3.2.3 Leaf net radiation per unit leaf area and photosynthetically active radiation

For a canopy layer i, the net radiative fluxes per unit leaf area for sunlit and shaded foliage, which are used in the calculation of leaf energy balance, are given by

$$R_i^{\mathrm{sun}} = \sum_k q_{i,k}^{\mathrm{sun,SW}} + \sum_l \left(q_{i,l}^{\mathrm{emit,LW}} + q_{i,l}^{\mathrm{abs,LW}} \right), \tag{14}$$

$$R_i^{\mathrm{sha}} = \sum_k q_{i,k}^{\mathrm{sha,SW}} + \sum_l \left(q_{i,l}^{\mathrm{emit,LW}} + q_{i,l}^{\mathrm{abs,LW}} \right). \tag{15}$$

Photosynthetically active radiation (PAR) corresponds to the portion of the shortwave spectrum that can be used by vegetation for photosynthesis. Using the PAR relevant spectral bands p, the PAR for the canopy layer i (in $\mu\mathrm{mol\,m^{-2}\,s^{-1}}$) is calculated for sunlit and shaded foliage as

$$\mathrm{PAR}_i^{\mathrm{sun}} = \sum_p q_{i,p}^{\mathrm{sun,SW}} \cdot \gamma_p^{\mathrm{PAR}}, \tag{16}$$

$$\mathrm{PAR}_i^{\mathrm{sha}} = \sum_p q_{i,p}^{\mathrm{sha,SW}} \cdot \gamma_p^{\mathrm{PAR}}, \tag{17}$$

where γ_p^{PAR} ($\mu\mathrm{mol\,J^{-1}}$) is a constant energy to photon conversion factor for band p.

3.2.4 Ground net radiation

Ground net radiation is required for calculating the surface energy balance. SPARTACUS solves for the ground net radiation components of direct ($Q_{\mathrm{ground},k}^{\mathrm{dir}}$) and diffuse ($Q_{\mathrm{ground},k}^{\mathrm{dif}}$) radiations from the unit direct beam and diffuse shortwave radiation forcing at the canopy top for a given spectral band k. The shortwave component ($Q_{\mathrm{ground}}^{\mathrm{SW}}$) is given by

$$Q_{\mathrm{ground}}^{\mathrm{SW}} = \sum_k \left[S_k^{\mathrm{dir}} \cdot Q_{\mathrm{ground},k}^{\mathrm{dir}} + S_k^{\mathrm{dif}} \cdot Q_{\mathrm{ground},k}^{\mathrm{dif}} \right]. \tag{18}$$

Similar to the longwave radiation solution for foliage, SPARTACUS provides net longwave radiation at the ground, which is calculated as the downward longwave radiation reaching the surface due to internal emissions from the regions above, minus the upward internal thermal emission from the ground ($R_{\mathrm{ground},l}^{\mathrm{emit}}$) and ground absorption from unit downwelling longwave from canopy top ($R_{\mathrm{ground},l}^{\mathrm{abs}}$) in spectral band l. Given L_l^{sky}, the longwave contribution to ground net radiation is

$$Q_{\mathrm{ground}}^{\mathrm{LW}} = \sum_l \left[R_{\mathrm{ground},l}^{\mathrm{emit}} + L_l^{\mathrm{sky}} \cdot R_{\mathrm{ground},l}^{\mathrm{abs}} \right]. \tag{19}$$

https://doi.org/10.5194/egusphere-2026-4875
Preprint. Discussion started: 21 September 2026

Finally, the ground net radiation (per unit ground area) is

$$Q^{\mathrm{net}}_{\mathrm{ground}} = Q^{\mathrm{SW}}_{\mathrm{ground}} + Q^{\mathrm{LW}}_{\mathrm{ground}}. \tag{20}$$

3.3 Canopy turbulence scheme accounting for the roughness sub-layer

Wind speed and aerodynamic conductance above and within the canopy are computed using the Harman and Finnigan RSL theory (Harman and Finnigan, 2007, 2008), which modifies the standard Monin–Obukhov flux–gradient relationships to account for the enhanced mixing at the canopy top. Our implementation of the scheme in a multilayer configuration follows Bonan et al. (2018). We note that a scheme was also implemented in the community Noah-MP single-layer configuration by Abolafia-Rosenzweig et al. (2021).

RSL corrected stability functions for momentum $\Psi_m^{\mathrm{H\&F}}(z)$ and scalars $\Psi_c^{\mathrm{H\&F}}(z)$ above the canopy are given by

$$\Psi_m^{\mathrm{H\&F}}(z) = -\psi_m\left(\frac{z-d^{\mathrm{veg}}}{L^{\mathrm{veg}}_{\mathrm{MO}}}\right) + \psi_m\left(\frac{h_c-d^{\mathrm{veg}}}{L^{\mathrm{veg}}_{\mathrm{MO}}}\right) + \widehat{\psi}_m(z) - \widehat{\psi}_m(h_c) + \frac{\mathrm{vkc}}{\beta}, \tag{21}$$

$$\Psi_c^{\mathrm{H\&F}}(z) = -\psi_c\left(\frac{z-d^{\mathrm{veg}}}{L^{\mathrm{veg}}_{\mathrm{MO}}}\right) + \psi_c\left(\frac{h_c-d^{\mathrm{veg}}}{L^{\mathrm{veg}}_{\mathrm{MO}}}\right) + \widehat{\psi}_c(z) - \widehat{\psi}_c(h_c), \tag{22}$$

where z is the height above the ground (m), h_c is the height of the canopy (m), $L^{\mathrm{veg}}_{\mathrm{MO}}$ is the Obukhov length (m), d^{veg} is the displacement height for the vegetated surface, vkc is the von Karman constant, β is defined as the ratio of friction velocity for the vegetated surface (u_*^{veg}) to the wind speed at h_c. ψ_m and ψ_c are the Monin-Obukhov stability functions, while $\widehat{\psi}_m(z)$ and $\widehat{\psi}_c(z)$ are the RSL integrals described in the scheme. An advantage of this RSL scheme is that it allows for the calculation of d^{veg} based on the canopy parameters and flow type. Further, roughness length for vegetation is eliminated by the introduction of β. Using $\Psi_m^{\mathrm{H\&F}}(z)$, the wind speed above the canopy is given by

$$u^{\mathrm{veg}}(z) = \frac{u_*^{\mathrm{veg}}}{\mathrm{vkc}}\left[\ln\left(\frac{z-d^{\mathrm{veg}}}{h_c-d^{\mathrm{veg}}}\right) + \Psi_m^{\mathrm{H\&F}}(z)\right], \quad z \geq h_c. \tag{23}$$

From the conservation of momentum at h_c, the theory provides an exponential profile for wind speed within the canopy:

$$u^{\mathrm{veg}}(z) = u^{\mathrm{veg}}(h_c)\cdot\exp\left(\frac{z-h_c}{l_m/\beta}\right), \quad z \leq h_c \tag{24}$$

where l_m is the within canopy mixing length scale.

$\Psi_c^{\mathrm{H\&F}}(z)$ and the within canopy wind speed can be used to calculate the vertical profile of aerodynamic conductance for scalars in the vegetated surfaces ($g_{\mathrm{a}}^{\mathrm{veg}}$) between adjacent canopy layers (z_i and z_{i+1}) from the surface up to the forcing height. Later, $g_{\mathrm{a}}^{\mathrm{veg}}$ is used in the canopy implicit solution to compute the scalar profiles. Above the canopy ($z \geq h_c$),

https://doi.org/10.5194/egusphere-2026-4875
Preprint. Discussion started: 21 September 2026

$$g_{\mathrm{a}}^{\mathrm{veg}}(z_i, z_{i+1}) = \frac{\rho u_*^{\mathrm{veg}} \times \mathrm{vkc}}{\ln\left(\frac{z_{i+1}-d^{\mathrm{veg}}}{z_i - d^{\mathrm{veg}}}\right) + \Psi_c^{\mathrm{H\&F}}(z_{i+1}) - \Psi_c^{\mathrm{H\&F}}(z_i)}, \tag{25}$$

where ρ is the molar density ($\mathrm{mol\,m^{-3}}$). Within the canopy ($z \leq h_c$), $g_{\mathrm{a}}^{\mathrm{veg}}$ is parameterized based on l_m/β as

$$\frac{1}{g_{\mathrm{a}}^{\mathrm{veg}}(z_i, z_{i+1})} = \frac{1}{\rho} \cdot \frac{\mathrm{Sc}}{\beta u_*^{\mathrm{veg}}} \left[\exp\left(-\frac{z_i - h_c}{l_m/\beta}\right) - \exp\left(-\frac{z_{i+1} - h_c}{l_m/\beta}\right)\right], \tag{26}$$

where Sc is the turbulent Schmidt number defined as the ratio of eddy diffusivities or turbulence length scales of momentum and scalars. The original Harman-Finnigan RSL theory is only valid for dense canopies where the ground is a major momentum sink. However, Bonan et al. (2018) further modified the parameterization to account for sparse canopies.

For the bare ground, the wind speed (u^{bare}) and aerodynamic conductance ($g_{\mathrm{a}}^{\mathrm{bare}}$) are calculated using Monin-Obukhov similarity theory. The wind profile above the surface is

$$u^{\mathrm{bare}}(z) = \frac{u_*^{\mathrm{bare}}}{\mathrm{vkc}} \left[\ln\left(\frac{z - d^{\mathrm{bare}}}{z_{0\mathrm{m}}^{\mathrm{bare}}}\right) - \psi_m\left(\frac{z - d^{\mathrm{bare}}}{L_{\mathrm{MO}}^{\mathrm{bare}}}\right) + \psi_m\left(\frac{z_{0\mathrm{m}}^{\mathrm{bare}}}{L_{\mathrm{MO}}^{\mathrm{bare}}}\right)\right], \tag{27}$$

where $z_{0\mathrm{m}}^{\mathrm{bare}}$ (set to $0.01\,\mathrm{m}$) is the bare ground roughness length of momentum and d^{bare} is the displacement height of the bare ground (set to $0\,\mathrm{m}$). Aerodynamic conductance between adjacent layers for the bare surface is calculated as

$$g_{\mathrm{a}}^{\mathrm{bare}}(z_i, z_{i+1}) = \frac{\rho u_*^{\mathrm{bare}} \times \mathrm{vkc}}{\ln\left(\frac{z_{i+1}-d^{\mathrm{bare}}}{z_i - d^{\mathrm{bare}}}\right) - \psi_c\left(\frac{z_{i+1}-d^{\mathrm{bare}}}{L_{\mathrm{MO}}^{\mathrm{bare}}}\right) + \psi_c\left(\frac{z_i - d^{\mathrm{bare}}}{L_{\mathrm{MO}}^{\mathrm{bare}}}\right)}. \tag{28}$$

For the calculation of aerodynamic conductance between the ground and midpoint of the first layer (z_1) for vegetated ($g_{\mathrm{a,ground}}^{\mathrm{veg}}$) and bare surface types ($g_{\mathrm{a,ground}}^{\mathrm{bare}}$), z_i is replaced by $z_{0\mathrm{c}}^{\mathrm{veg/bare}}$ ($= 0.1 \cdot z_{0\mathrm{m}}^{\mathrm{veg/bare}}$) and z_{i+1} by z_1 in equations 26 and 28, respectively. Here, $z_{0\mathrm{m}}^{\mathrm{veg}}$ is the ground roughness length of momentum at the vegetated surface, which is set equal to $z_{0\mathrm{m}}^{\mathrm{bare}}$ in our implementation. At the top model layer, the same equations for aerodynamic conductance (equations 25 and 28) are used, but with $z_{i+1} = z_{\mathrm{ref}}$, where z_{ref} is the forcing height (m).

3.4 Canopy implicit solution

We solve the multilayer canopy following the implicit solution by Ryder et al. (2016), which was revised by Bonan et al. (2018). The formulation solves for the air temperature and specific humidity within and above the canopy for both vegetated and bare land surfaces separately ($\theta_{\mathrm{veg/bare}}$ in K and $\mathrm{qv}_{\mathrm{veg/bare}}$ in $\mathrm{mol\,mol^{-1}}$), as well as the leaf temperatures of sunlit ($T_{\mathrm{l,sun}}$, K) and shaded ($T_{\mathrm{l,sha}}$, K) foliage at time $n+1$ using the canopy state at time n. The canopy is integrated with 5-minute sub-steps embedded within the forcing time step (e.g., 12 sub-steps for hourly forcing). These sub-steps are required because the canopy parameters (leaf temperature, stomatal conductance, longwave radiation, aerodynamic conductance, etc.) depend

https://doi.org/10.5194/egusphere-2026-4875
Preprint. Discussion started: 21 September 2026

strongly on each other and evolve within a single forcing time interval (typically one hour). Thus, updating these parameters every 5 minutes and averaging them over the forcing time step provides a stable and smooth solution for the canopy.

With reference to Figure 3, for each canopy layer i in the vegetated surface, the prognostic air temperature ($\theta^{n+1}_{\mathrm{veg},i}$) and specific humidity ($\mathrm{qv}^{n+1}_{\mathrm{veg},i}$) at time $n+1$ are obtained from a balance between the layer storage over the sub-time step (Δt, seconds), vertical divergence of turbulent fluxes, and the sources and sinks from sunlit and shaded foliage in the i^{th} layer as

$$\begin{aligned}\rho c_\mathrm{p}\Delta z\left(\frac{\theta^{n+1}_{\mathrm{veg},i}-\theta^{n}_{\mathrm{veg},i}}{\Delta t}\right)+c_\mathrm{p}\left(\theta^{n+1}_{\mathrm{veg},i}-\theta^{n+1}_{\mathrm{veg},i-1}\right)\cdot g^{\mathrm{veg}}_{\mathrm{a},i-1}+c_\mathrm{p}\left(\theta^{n+1}_{\mathrm{veg},i}-\theta^{n+1}_{\mathrm{veg},i+1}\right)\cdot g^{\mathrm{veg}}_{\mathrm{a},i}\\ =2c_\mathrm{p}\left(T^{n+1}_{\mathrm{l,sun},i}-\theta^{n+1}_{\mathrm{veg},i}\right)\cdot g^{\mathrm{bh}}_i\cdot f^{\mathrm{sun}}_i\cdot \mathrm{LAI}_i+2c_\mathrm{p}\left(T^{n+1}_{\mathrm{l,sha},i}-\theta^{n+1}_{\mathrm{veg},i}\right)\cdot g^{\mathrm{bh}}_i\cdot\left(1-f^{\mathrm{sun}}_i\right)\cdot \mathrm{LAI}_i,\end{aligned}\tag{29}$$

$$\begin{aligned}\rho\Delta z\left(\frac{\mathrm{qv}^{n+1}_{\mathrm{veg},i}-\mathrm{qv}^{n}_{\mathrm{veg},i}}{\Delta t}\right)+\left(\mathrm{qv}^{n+1}_{\mathrm{veg},i}-\mathrm{qv}^{n+1}_{\mathrm{veg},i-1}\right)\cdot g^{\mathrm{veg}}_{\mathrm{a},i-1}+\left(\mathrm{qv}^{n+1}_{\mathrm{veg},i}-\mathrm{qv}^{n+1}_{\mathrm{veg},i+1}\right)\cdot g^{\mathrm{veg}}_{\mathrm{a},i}\\ =\left[\mathrm{qv}_\mathrm{sat}\left(T^{n+1}_{\mathrm{l,sun},i}\right)-\mathrm{qv}^{n+1}_{\mathrm{veg},i}\right]\cdot g^{\mathrm{l,sun}}_i\cdot f^{\mathrm{sun}}_i\cdot\mathrm{LAI}_i\\ +\left[\mathrm{qv}_\mathrm{sat}\left(T^{n+1}_{\mathrm{l,sha},i}\right)-\mathrm{qv}^{n+1}_{\mathrm{veg},i}\right]\cdot g^{\mathrm{l,sha}}_i\cdot\left(1-f^{\mathrm{sun}}_i\right)\cdot\mathrm{LAI}_i,\end{aligned}\tag{30}$$

where c_p is the moist air specific heat at constant pressure ($\mathrm{J\,mol^{-1}\,K^{-1}}$), Δz is the layer thickness (m), and $\mathrm{qv}_\mathrm{sat}(T^{n+1}_{\mathrm{l,sun},i})$ and $\mathrm{qv}_\mathrm{sat}(T^{n+1}_{\mathrm{l,sha},i})$ are the saturated vapor pressures at sunlit and shaded foliage temperatures at time $n+1$. g^{bh}_i is the leaf boundary layer conductance to heat ($\mathrm{mol\,m^{-2}\,s^{-1}}$). $g^{\mathrm{tot,sun}}_i$ and $g^{\mathrm{tot,sha}}_i$ are the total conductance to transpiration for sunlit and shaded foliage ($\mathrm{mol\,m^{-2}\,s^{-1}}$), respectively. These are calculated as $\frac{1}{g^{\mathrm{tot,sun/sha}}_i}=\frac{1}{g^{\mathrm{bv}}_i}+\frac{1}{g^{\mathrm{sw,sun/sha}}_i}$, where g^{bv}_i is the leaf boundary layer conductance for water vapor ($\mathrm{mol\,m^{-2}\,s^{-1}}$) and $g^{\mathrm{sw,sun/sha}}_i$ are the stomatal conductance of sunlit or shaded foliage ($\mathrm{mol\,m^{-2}\,s^{-1}}$). The effective leaf conductance for water vapor ($g^{\mathrm{l,sun/sha}}_i$) are calculated as $g^{\mathrm{l,sun/sha}}_i=g^{\mathrm{tot,sun/sha}}_i\times f^i_{\mathrm{wet}}+g^{\mathrm{bv}}_i\times f^i_{\mathrm{dry}}$, where f^i_{wet} and f^i_{dry} are the canopy wet and dry fractions calculated from the canopy water interception. $\mathrm{qv}_\mathrm{sat}(T^{n+1}_{\mathrm{l,sun},i})$ [and likewise, $\mathrm{qv}_\mathrm{sat}(T^{n+1}_{\mathrm{l,sha},i})$] is linearized around the sunlit foliage temperature at time n ($T^{n}_{\mathrm{l,sun},i}$) as

$$\begin{aligned}\mathrm{qv}_\mathrm{sat}\left(T^{n+1}_{\mathrm{l,sun},i}\right)=\mathrm{qv}_\mathrm{sat}\left(T^{n}_{\mathrm{l,sun},i}\right)\\ +\frac{\mathrm{d}\left[\mathrm{qv}_\mathrm{sat}\left(T^{n}_{\mathrm{l,sun},i}\right)\right]}{\mathrm{d}T}\left(T^{n+1}_{\mathrm{l,sun},i}-T^{n}_{\mathrm{l,sun},i}\right).\end{aligned}\tag{31}$$

To close the system of $\theta^{n+1}_{\mathrm{veg},i}$ and $\mathrm{qv}^{n+1}_{\mathrm{veg},i}$, additional equations for $T^{n+1}_{\mathrm{l,sun},i}$ and $T^{n+1}_{\mathrm{l,sha},i}$ are required. These come from the leaf energy balance:

$$\begin{aligned}R^{\mathrm{sun}}_i=c_\mathrm{l}\left(\frac{T^{n+1}_{\mathrm{l,sun},i}-T^{n}_{\mathrm{l,sun},i}}{\Delta t}\right)+2c_\mathrm{p}\left(T^{n+1}_{\mathrm{l,sun},i}-\theta^{n+1}_{\mathrm{veg},i}\right)\cdot g^{\mathrm{bh}}_i\\ +\lambda\left[\mathrm{qv}_\mathrm{sat}\left(T^{n+1}_{\mathrm{l,sun},i}\right)-\mathrm{qv}^{n+1}_{\mathrm{veg},i}\right]\cdot g^{\mathrm{l,sun}}_i,\end{aligned}\tag{32}$$

https://doi.org/10.5194/egusphere-2026-4875
Preprint. Discussion started: 21 September 2026

where c_l is the leaf heat capacity ($\mathrm{J\,m^{-2}\,K^{-1}}$) and λ is the latent heat of vaporization ($\mathrm{J\,mol^{-1}}$). $T^{n+1}_{\mathrm{l,sha},i}$ is similarly calculated from the energy budget of the shaded foliage.

300 At the top of the canopy, $\theta^{n+1}_{\mathrm{veg},i}$ and $\mathrm{qv}^{n+1}_{\mathrm{veg},i}$ are replaced by the forcing temperature ($\theta^{n+1}_{\mathrm{ref}}$) and humidity ($\mathrm{qv}^{n+1}_{\mathrm{ref}}$), respectively. At the bottom layer, the sensible and latent heat flux from the soil are the boundary conditions. These are integrated in the implicit solution through the surface energy balance equation given by

$$\begin{aligned} Q^{\mathrm{net}}_{\mathrm{ground}} = c_\mathrm{p}\left(T^{n+1}_{\mathrm{veg,ground}} - \theta^{n+1}_{\mathrm{veg},1}\right)\cdot g^{\mathrm{veg}}_{\mathrm{a,ground}} \\ + \lambda\left\{\mathrm{rh}^{\mathrm{veg}}_{\mathrm{ground}}\left[\mathrm{qv}_{\mathrm{sat}}\left(T^{n+1}_{\mathrm{veg,ground}}\right) - \mathrm{qv}^{n+1}_{\mathrm{veg},1}\right]\cdot g^{\mathrm{veg}}_{\mathrm{tot,ground}}\right\} + G^{n+1}_{\mathrm{veg}}, \end{aligned} \tag{33}$$

where $T^{n+1}_{\mathrm{veg,ground}}$ is the surface temperature (K) of the vegetated surface at $n+1$, G^{n+1}_{veg} is the ground heat flux ($\mathrm{W\,m^{-2}}$) 305 at the vegetated surface, $g^{\mathrm{veg}}_{\mathrm{tot,ground}}$ is the total conductance for soil evaporation ($\mathrm{mol\,m^{-2}\,s^{-1}}$) calculated as $\frac{1}{g^{\mathrm{veg}}_{\mathrm{tot,ground}}} = \frac{1}{g^{\mathrm{veg}}_{\mathrm{soil}}} + \frac{1}{g^{\mathrm{veg}}_{\mathrm{a,ground}}}$, where $g^{\mathrm{veg}}_{\mathrm{soil}}$ is the soil conductance for the vegetated surface and is calculated following Sakaguchi and Zeng (2009). $\mathrm{qv}_{\mathrm{sat}}(T^{n+1}_{\mathrm{veg,ground}})$ is linearized around the vegetated surface temperature at n ($T^{n}_{\mathrm{veg,ground}}$). $\mathrm{rh}^{\mathrm{veg}}_{\mathrm{ground}}$ is the relative humidity at ground for the vegetated surface ($-$) and is calculated as

$$\mathrm{rh}^{\mathrm{veg}}_{\mathrm{ground}} = e^{\left(\frac{\Psi_{\mathrm{sfc}}\times \mathrm{grav}}{273.15\times T^{n}_{\mathrm{veg,ground}}}\right)}, \tag{34}$$

310 where Ψ_{sfc} is the soil matric potential of the surface (m), grav is the gravitational constant ($=9.81\,\mathrm{m\,s^{-2}}$). G^{n+1}_{veg} is calculated as a part of the implicit solution but requires the soil temperature of the first layer soil at n. Equations 29, 30, 32 (and similar leaf energy budget for shaded foliage), and 33 form a set of linear equations for $\theta^{n+1}_{\mathrm{veg},i}$, $\mathrm{qv}^{n+1}_{\mathrm{veg},i}$, $T^{n+1}_{\mathrm{l,sun},i}$ and $T^{n+1}_{\mathrm{l,sha},i}$. These can be arranged into a tridiagonal matrix that can be solved using the Gauss elimination method.

The solution for the bare ground follows a similar method, but is largely simplified as $\mathrm{LAI}_i = 0$, thus there are no foliage 315 source or sink terms in the layer budgets. The aerodynamic conductances for bare ground are $g^{\mathrm{bare}}_{\mathrm{a}}(z_i, z_{i+1})$ and $g^{\mathrm{bare}}_{\mathrm{a,ground}}$. The soil conductance and surface relative humidity for bare ground are computed analogously using the bare ground surface temperature.

4 Subsurface processes in Noah-MP-ML^2

The sub-surface grid is defined by prescribing the number of soil layers (N_s) and the thickness of the top soil layer ($\Delta z_{\mathrm{s},1}$). 320 The remaining soil layer thickness follows a geometric progression $\Delta z_{\mathrm{s},i} = \Delta z_{\mathrm{s},1}\cdot r_\mathrm{s}^{i-1}$ such that $\sum_{i=1}^{N_\mathrm{s}}\Delta z_{\mathrm{s},i} = Z_{\mathrm{s,max}}$, where $Z_{\mathrm{s,max}}$ is the total soil depth. The common ratio r_s is obtained numerically using a secant method. For the present case, we use $N_\mathrm{s} = 20$, $\Delta z_{\mathrm{s},1} = 1\,\mathrm{cm}$ and $Z_{\mathrm{s,max}} = 200\,\mathrm{cm}$. The resulting sub-surface grid is presented in Appendix A.

In addition to this geometric sub-surface grid, the model can also be configured to use the standard 4-layer community Noah-MP soil grid with thicknesses of 10, 30, 60, and 100 cm. When the community Noah-MP sub-surface grid is selected, 325 the existing community Noah-MP sub-surface parameterizations are used. However, at present, only the Schaake scheme

https://doi.org/10.5194/egusphere-2026-4875
Preprint. Discussion started: 21 September 2026

(Schaake et al., 1996) is implemented to calculate the soil water infiltration and drainage, which is also the default scheme in the community Noah-MP model. When the 20-layer soil configuration is used, the soil heat diffusion solver is the same as the community Noah-MP model, but a more detailed Richard's equation solver is used (described in section 4.3).

4.1 Soil thermal and hydraulic properties

Soil thermal properties are computed following the community Noah-MP model. The soil thermal conductivity (κ, $\mathrm{W\,m^{-1}\,K^{-1}}$) and volumetric soil heat capacity (C_s, $\mathrm{J\,m^{-3}\,K^{-1}}$) vary with soil liquid water content. Kersten number-based linear interpolation is used to compute κ (Peters-Lidard et al., 1998) as

$$\kappa = K_\mathrm{e} \cdot (\kappa_\mathrm{sat} - \kappa_\mathrm{dry}) + \kappa_\mathrm{dry}, \tag{35}$$

where κ_sat and κ_dry are the saturated and dry thermal conductivities, K_e $(-)$ is the Kersten number varies between 0 and 1 depending on the soil texture, water content, and water phase. C_s is calculated as the volume weighted sum of the heat capacity of soil solids, water, ice, and air as

$$C_\mathrm{s} = \theta_\mathrm{liq} \cdot C_\mathrm{liq} + \theta_\mathrm{ice} \cdot C_\mathrm{ice} + (1 - \theta_\mathrm{sat}) \cdot C_\mathrm{soil} + (\theta_\mathrm{sat} - \theta_\mathrm{tot}) \cdot C_\mathrm{a}, \tag{36}$$

where θ_liq, θ_ice and θ_tot are the liquid, ice, and total soil moisture, respectively, θ_sat is porosity, and C_liq, C_ice, C_soil and C_a are volumetric heat capacities of liquid, ice, soil solids, and air, respectively.

The soil hydraulic properties are necessary for solving Richards equation. When the 4-layer community Noah-MP sub-surface scheme is selected, the model uses the community Noah-MP's default Richards equation solver with water retention curves and functional forms of hydraulic conductivity derived from Campbell (1974), and parameters for different soil types are from Clapp and Hornberger (1978). However, when the 20-layer sub-surface grid is used, the soil hydraulic properties are calculated using the van Genuchten (1980) water retention model. Using the van Genuchten formulation, matric potential (ψ in cm) is computed as

$$\psi = -\frac{\left(S_\mathrm{e}^{-1/m_\mathrm{VG}} - 1\right)^{1/n_\mathrm{VG}}}{\alpha_\mathrm{VG}}, \tag{37}$$

where n_VG $(-)$ is the pore size distribution parameter, α_VG ($\mathrm{cm^{-1}}$) is the inverse air entry potential, $m_\mathrm{VG} = 1 - \frac{1}{n_\mathrm{VG}}$ and S_e is the effective saturation defined as

$$S_\mathrm{e} = \frac{\theta_\mathrm{liq} - \theta_\mathrm{r,VG}}{\theta_\mathrm{s,VG} - \theta_\mathrm{r,VG}}, \tag{38}$$

where $\theta_\mathrm{r,VG}$ ($\mathrm{m^3\,m^{-3}}$) is the residual volumetric water content and $\theta_\mathrm{s,VG}$ ($\mathrm{m^3\,m^{-3}}$) is the saturated the volumetric water content. The hydraulic conductivity (K_VG, $\mathrm{cm\,s^{-1}}$) and $\mathrm{d}\theta_\mathrm{liq}/\mathrm{d}\psi$ are given by

https://doi.org/10.5194/egusphere-2026-4875
Preprint. Discussion started: 21 September 2026

$$K_{\mathrm{VG}} = K_{\mathrm{VG,sat}} \cdot \sqrt{S_{\mathrm{e}}} \cdot \left\{1 - \left(1 - s_{\mathrm{e}}^{1/m_{\mathrm{VG}}}\right)^{m_{\mathrm{VG}}}\right\}^2, \tag{39}$$

$$\frac{\mathrm{d}\theta_{\mathrm{liq}}}{\mathrm{d}\psi} = \frac{\alpha_{\mathrm{VG}} \cdot n_{\mathrm{VG}} \cdot m_{\mathrm{VG}} \cdot (\theta_{\mathrm{s,VG}} - \theta_{\mathrm{r,VG}}) \cdot (\alpha_{\mathrm{VG}}|\psi|)^{n_{\mathrm{VG}}-1}}{\{1 + (\alpha_{\mathrm{VG}}|\psi|)^{n_{\mathrm{VG}}}\}^{m_{\mathrm{VG}}+1}}, \tag{40}$$

where $K_{\mathrm{VG,sat}}$ is the saturated hydraulic conductivity ($\mathrm{cm\,s^{-1}}$). The van Genuchten parameters (subscripted as VG) vary with soil types, and the standard values from Carsel and Parrish (1988) are used.

4.2 Root profile and soil moisture stress to transpiration

When the 20-layer sub-surface grid is used, the vertical distribution of roots follows the exponential formulation by Jackson et al. (1996), where the cumulative root fraction at depth z_{s} (cm) is given by

$$F(z_{\mathrm{s}}) = 1 - \beta_{\mathrm{s}}^{z_{\mathrm{s}}}, \tag{41}$$

where β_{s} $(-)$ is the vegetation-type dependent parameter. For the discretized soil column, the root fraction in layer i is calculated as the difference between the cumulative root fraction and is normalized so that the sum of layer-wise root fractions in the soil column is equal to one. An effective rooting depth is defined as the depth containing $99.5\,\%$ of the cumulative root mass, and the soil layers below this depth are excluded from root water uptake. When using the community Noah-MP sub-surface, the number of soil layers in which roots exist is prescribed in the lookup table for different vegetation types.

When the 20-layer sub-surface grid with detailed Richards equation solver is used, β_{soil} (which scales layer-wise $V_{c,\max}$ in stomatal conductance calculation) is calculated using the root fraction and layer-wise soil wetness factor W_i $(-)$ as

$$W_i = \frac{1 - \psi_i/\psi_{\mathrm{wilt},i}}{1 + \psi_{\mathrm{sat},i}/\psi_{\mathrm{wilt},i}}, \tag{42}$$

where ψ_i and $\psi_{\mathrm{sat},i}$ are the layer-wise matric potentials and saturated matric potentials, respectively, which are calculated using the van Genuchten formulation. $\psi_{\mathrm{wilt},i}$ is the layer-wise matric potential at wilting point, which is taken to be $-15000\,\mathrm{cm}$. β_{soil} is finally calculated as

$$\beta_{\mathrm{soil}} = \sum_{i=1}^{N_{\mathrm{root}}} R_i \cdot W_i, \tag{43}$$

where N_{root} is the number of rooted layers and R_i is the root fraction. In the community Noah-MP 4-layer soil grid, β_{soil} is calculated as

https://doi.org/10.5194/egusphere-2026-4875
Preprint. Discussion started: 21 September 2026

$$\beta_{\mathrm{soil}} = \sum_{i=1}^{N_{\mathrm{root}}} \left(\frac{\Delta z_{\mathrm{s},i}}{Z_{\mathrm{s},i}} \right) \cdot W_i, \tag{44}$$

where $\Delta z_{\mathrm{s},i}$ (m) is the layer-wise thickness of the soil layer and $Z_{\mathrm{s},i}$ is the depth of the deepest-rooted layer (m). W_i is calculated as before, but with Campbell (1974) water retention formulation.

4.3 Soil water diffusion

The Noah-MP-ML^2 solves the mixed form of the 1-D Richards equation to calculate water infiltration and to update the volumetric soil liquid water content (Richards, 1931). The governing equation for a soil column where the depth z (cm) is positive downwards is

$$\frac{\partial \theta_{\mathrm{liq}}}{\partial t} = \frac{\partial}{\partial z} \left[K_{\mathrm{VG}} \left(\theta_{\mathrm{liq}} \right) \cdot \frac{\partial \psi}{\partial z} \right] - \frac{\partial K_{\mathrm{VG}}}{\partial z} - S_{\mathrm{s}}(z), \tag{45}$$

where $S_{\mathrm{s}}(z)$ represents the sink from soil evaporation (for top layers), root water uptake (if roots exist), or both. The transpiration flux sink component of $S_{\mathrm{s}}(z)$ for soil layer i is given by

$$S_{\mathrm{s,trans},i} = \text{Transpiration flux} \times \frac{R_i \cdot W_i}{\beta_{\mathrm{soil}}}, \tag{46}$$

We use Picard's iteration method to numerically solve the Richards equation, where we linearize $\theta_{\mathrm{liq},i}^{n+1,m+1}$ using the $\theta_{\mathrm{liq},i}^{n+1,m}$ and specific soil moisture capacity C_i for the soil layer i, allowing for the conservation of mass following Celia et al. (1990):

$$\theta_{\mathrm{liq},i}^{n+1,m+1} = \theta_{\mathrm{liq},i}^{n+1,m} + C_i^{n+1,m} \cdot \left(\psi_i^{n+1,m+1} - \psi_i^{n+1,m} \right), \tag{47}$$

where

$$C_i^{n+1,m} = \left. \frac{\partial \theta_{\mathrm{liq},i}}{\partial \psi_i} \right|_{n+1,m}. \tag{48}$$

K_{VG} is calculated as the arithmetic mean of adjacent nodal values as

$$K_{\mathrm{VG},i+1/2}^{n+1,m+1} = \frac{1}{2} \left(K_{\mathrm{VG},i}^{n+1,m} + K_{\mathrm{VG},i+1}^{n+1,m} \right), \tag{49}$$

where n is the time and m is the iteration number. After linearization, we solve for the system the residue under relaxation (Paniconi and Putti, 1994): $\psi_i^{n+1,m+1} = \psi_i^{n+1,m} + \omega \Delta \psi_i^{m+1}$, where $0 < \omega < 1$ is the damping factor. The iteration continues until $|\Delta \psi_i|$ falls below a prescribed tolerance. Additionally, a water balance check is enforced after each successful iteration as

https://doi.org/10.5194/egusphere-2026-4875
Preprint. Discussion started: 21 September 2026

$$\Delta\text{Storage} \approx \left(\text{Infiltration} - \text{Drainage} - \text{Evaporation} - \sum \text{Transpiration}_i\right) \cdot \Delta t, \quad (50)$$

where Δt is the solver time step. Free drainage is taken as the bottom boundary condition. At the surface, the solver supports three boundary conditions depending on the water availability and surface ponding: (i) a prescribed flux (Neumann) condition when the supply is below infiltration capacity, (ii) a prescribed head condition at saturation (Dirichlet) when the surface is exactly saturating without ponding, and (iii) a ponded head condition when surface water storage exists, where the surface head is set by pond depth. Infiltration is limited by the instantaneous hydraulic conductivity of the top layer, and any excess supply is stored as ponding. When the pond storage exceeds a prescribed maximum, the excess is released as runoff.

To maintain the numerical stability and convergence of the solver, especially during a strong wetting front, the sub-surface column is non-uniformly vertically discretized as discussed previously. The Richards solver uses an adaptive sub-stepping (Kavetski et al., 2001). Within each forcing interval, Δt is increased by a factor of 1.5 when the previous iteration converges in less than 10 iterations and is halved when either the tolerance or water-balance criterion fails to converge within 50 iterations.

Under weak Picard damping ($\omega = 0.8$), the Richards solver frequently fails to recover from a dry soil state after rainfall. To enable recovery, ω is adaptively reduced to 0.4. In addition, prescribing the wilting point too close to the residual soil moisture for coarse-textured soils prevents re-wetting despite damping. Introducing a modest separation between residual and wilting soil moisture ($\approx 0.005\,\mathrm{m^3\,m^{-3}}$) enabled realistic recovery in most of the cases we tested. Excessive root density concentrated in near-surface layers, which is controlled by the Jackson β_s parameter further exacerbated surface drying and hindered recovery. The adaptive damping strategy is applied only when soils approached extreme dryness and deactivated once moisture recovered. Finally, the cumulative water balance error is tracked over the complete model run to ensure stable behavior of the solver. For the simulations that activated adaptive damping during testing of the solver, we did notice increased cumulative water balance error.

The 1-D Richards equation solver described above was tested for a constant head configuration to simulate infiltration in Yolo light clay following the benchmark experiment of Haverkamp et al. (1977). Two numerical configurations were evaluated: (i) the soil column was discretized using a uniform $1\,\mathrm{cm}$ vertical grid and a fixed time step of 10 seconds (high resolution reference simulation), and (ii) an adaptive time step Richards solved on a geometrically stretched non-uniform grid where Δt_max capped at 3600 seconds. Soil liquid water profiles, cumulative infiltration, and computational time were compared between the two configurations. The simulated moisture profiles at 10^4, 10^5, 5×10^5 and 10^6 seconds are shown in Figure 6a alongside the analytical solution of Haverkamp et al. (1977), while Figure 6b presents the corresponding cumulative infiltration. The total runtime for each configuration is reported in the Figure caption. The adaptive time step solver on the stretched grid performs well in terms of the soil liquid water profiles and cumulative infiltration (Figure 6). The differences seen between the adaptive time step and high-resolution solver are primarily due to the stretched grid and not due to adaptive time stepping. Thus, it is important to add more shallow layers near the surface to calculate the soil water diffusion correctly.

https://doi.org/10.5194/egusphere-2026-4875
Preprint. Discussion started: 21 September 2026

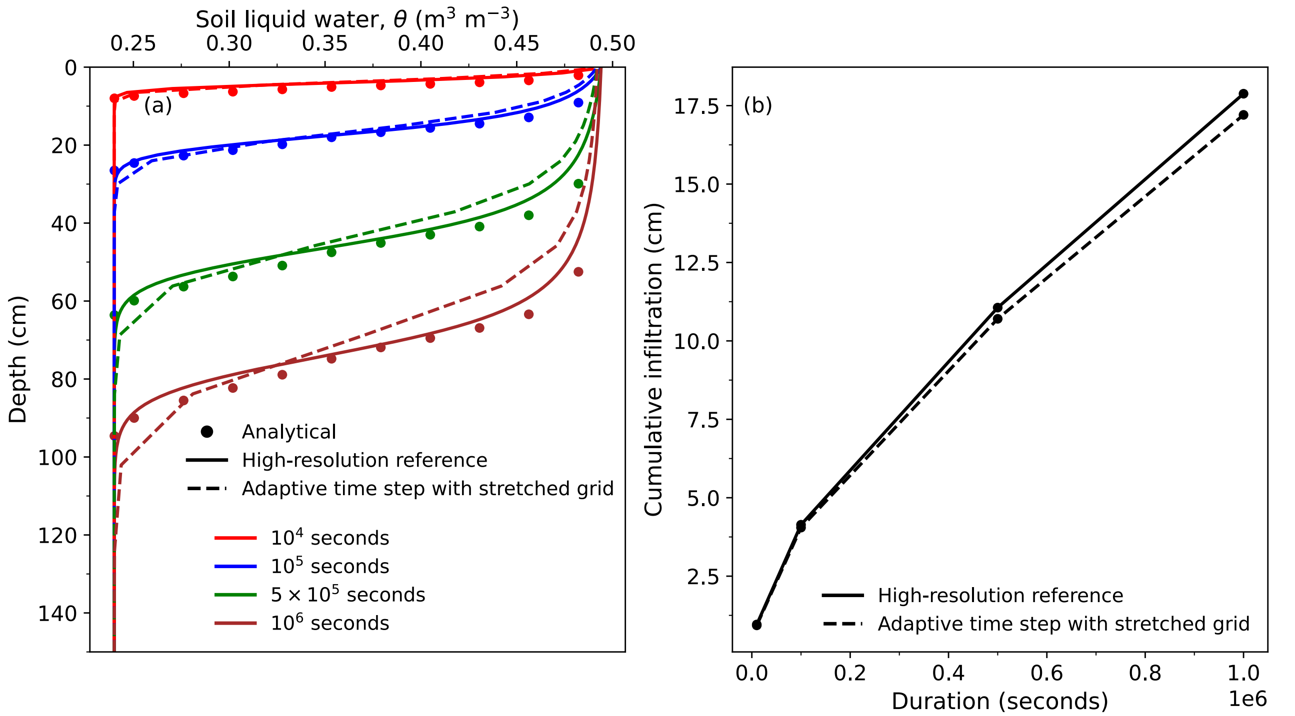

Figure 6. Richards equation with van Genuchten hydraulic properties for Yolo light clay with initial column soil liquid water $= 0.24\,\mathrm{m^3\,m^{-3}}$. Two experiments were performed: (i) a high-resolution reference that uses $1\,\mathrm{cm}$ layer thicknesses (200 layers) and 10 second time steps, and (ii) Adaptive time step on a vertically stretched grid (20 layers). van Genuchten parameters: $n_{\mathrm{VG}} = 1.43$, $\alpha_{\mathrm{VG}} = 0.026\,\mathrm{cm^{-1}}$, $\theta_{\mathrm{r,VG}} = 0.124\,\mathrm{m^3\,m^{-3}}$, $\theta_{\mathrm{s,VG}} = 0.495\,\mathrm{m^3\,m^{-3}}$ and $K_{\mathrm{VG}}$was calculated following Haverkamp et al. (1977). (a) Soil moisture profiles for both the experiments and the analytical solution after a time lapse of 10^4, 10^5, 5×10^5 and 10^6 seconds. (b) Cumulative infiltration (in cm) after 10^4, 10^5, 5×10^5 and 10^6 seconds. Offline model execution time: 6.8, 61.5, 278.7, 557.7 seconds and 0.8, 2.7, 7.2, 11.5 seconds for high resolution and adaptive time step experiments, respectively.

4.4 Soil heat diffusion

The soil temperature (T_{soil}) is updated by solving the 1-D heat diffusion equation following the community Noah-MP implementation (He et al., 2023b; Niu et al., 2011). The heat diffusion equation solved is

$$C_{\mathrm{s}} \cdot \frac{\partial T_{\mathrm{soil}}}{\partial t} = \frac{\partial}{\partial z}\left(\kappa \cdot \frac{\partial T_{\mathrm{soil}}}{\partial z}\right). \tag{51}$$

At each model step, layer-wise thermal conductivity and volumetric heat capacity are computed. The heat diffusion equation is discretized on the vertically stretched grid to form a tridiagonal linear system that is solved for temperature increments. The system is advanced using a fully implicit backward-Euler scheme, which is unconditionally stable for time stepping and the

https://doi.org/10.5194/egusphere-2026-4875
Preprint. Discussion started: 21 September 2026

non-uniform grid used in the study. At the upper boundary, a prescribed ground heat flux (Neumann condition) is applied, while at the lower boundary, soil temperature is prescribed at $8\,\mathrm{m}$ depth (Ek et al., 2003).

5 Noah-MP-ML^2 Model flow

The Noah-MP-ML^2 model flowchart is shown in Figure 7. The model first reads namelist options and initializes configuration, forcing, water, and energy state variables following the community Noah-MP v5 framework (He et al., 2023b). Domain static attributes (e.g., canopy height, LAI, leaf geometry) are then assigned, after which the canopy and soil vertical grids are constructed, and model parameters are prescribed (e.g., van Genuchten hydraulic parameters, soil thermal parameters, ground albedo, and leaf radiative properties). Next, atmospheric forcing is read from a NetCDF file containing surface pressure (Pa), air temperature (K), specific humidity ($\mathrm{kg\,kg^{-1}}$), wind speed ($\mathrm{m\,s^{-1}}$), cosine of solar zenith angle ($-$), shortwave radiation ($\mathrm{W\,m^{-2}}$) in visible/infrared bands separated into direct and diffuse components, incoming longwave radiation ($\mathrm{W\,m^{-2}}$), and precipitation rate ($\mathrm{mm\,s^{-1}}$). The number of model sub-steps per forcing interval is computed from the forcing timestep and the internal model sub-step (60 and 5 minutes in this study, respectively).

The simulation advances by looping over sub-grid tiles and stepping forward in time using the forcing data. At each forcing time step, shortwave radiative transfer inputs (e.g., extinction coefficients) are updated, and the canopy shortwave radiation solution is computed. The model then performs an internal loop over sub-steps where within each sub-step processes are evaluated in the following order: (1) ground/soil thermal properties, (2) canopy interception, (3) root water uptake and transpiration stress, (4) longwave radiative transfer, (5) canopy radiative diagnostics needed for leaf energy balance calculation, (6) leaf boundary layer conductance (for heat, water vapor, CO_2), (7) leaf heat capacity, (8) leaf vertical nitrogen profile, (9) photosynthesis, (10) canopy turbulence and within-canopy scalar, (11) subsurface processes, and (12) canopy evaporation. Within the subsurface module, soil temperature is updated by solving the 1-D heat diffusion equation over the sub-step. The soil moisture is updated by solving the Richards equation with adaptive internal time stepping ($\Delta t \leq \mathrm{substep}$). Finally, the canopy profiles and fluxes are aggregated over the forcing interval. Of the multilayer canopy process formulations, canopy interception and processes 6–10 follow CLM-ml v0 (Bonan et al., 2018). Note that when Noah-MP 4-layer sub-surface is selected, the default Noah-MP Richards equation solver is used.

6 Model evaluation

Although the model allows for multiple sub-grid tiles through an external landcover loop, the present study evaluates a single vegetated tile that occupies the full grid cell. Noah-MP-ML^2 was evaluated at five forest FLUXNET sites with different plant function types, soils, and background climates. Table 1 provides the details on the FLUXNET sites. The FLUXNET datasets were post-processed to filter for only the time periods when high-confidence data were available. Based on the data availability, we decided the simulation start and end dates. All the FLUXNET data were aggregated to 1 hour temporal resolution. Additionally, the Richards equation fails when $\theta_{\mathrm{liq}} \leq \theta_{\mathrm{r,VG}}$ due to soil water freezing. The current model also does not have

https://doi.org/10.5194/egusphere-2026-4875
Preprint. Discussion started: 21 September 2026

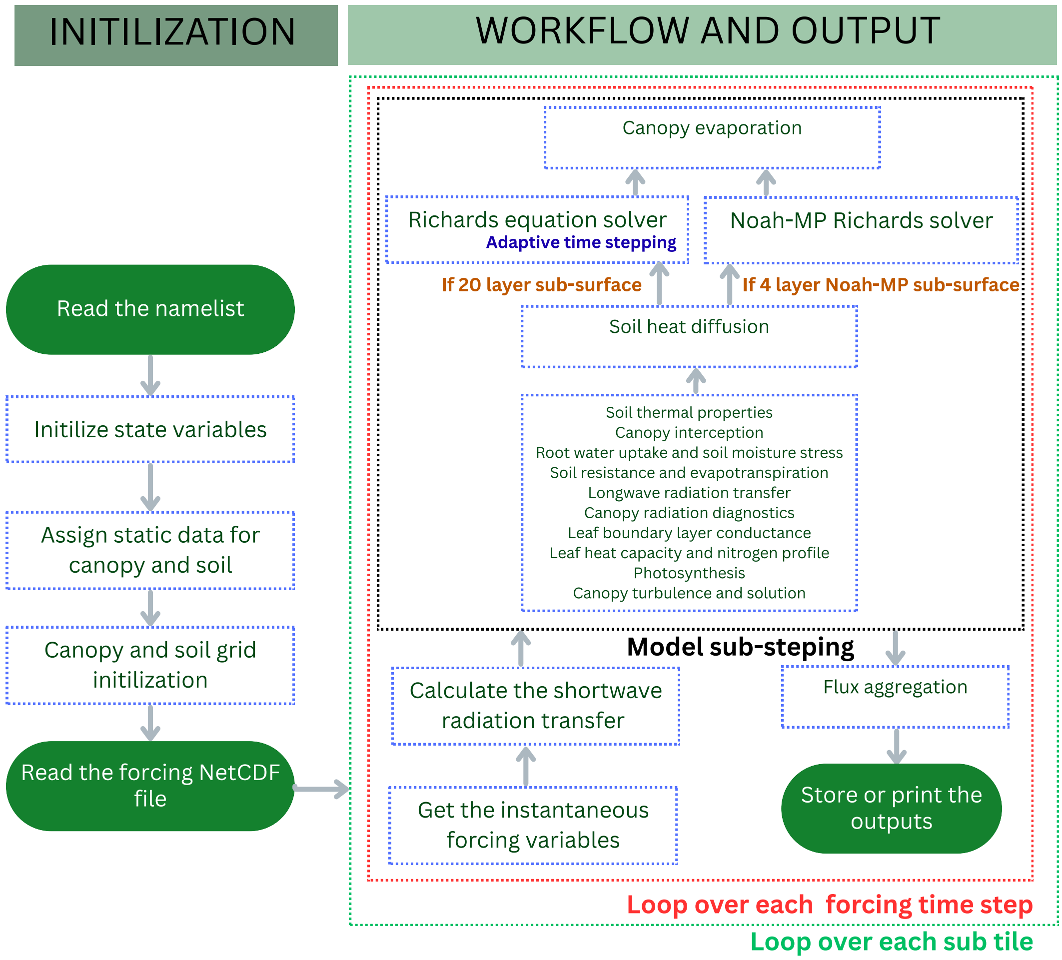

Figure 7. Model flowchart that shows how the inputs are read, the order in which the model executes, state variable aggregation, and output storage. Note: not all processes are shown in this Figure.

snow-related processes, which will be included in the future. Thus, we further narrowed our simulation time period to the warm months.

The model was initialized using the observed values for both the canopy and soil. The observed θ_{liq} and soil temperatures were interpolated onto the 20-layer or the 4-layer sub-surface grids, depending on the choice of the sub-surface model. However, at DE-HAI, US-MMS, and AU-Tum sites, deeper θ_{liq} and soil temperatures were not available. Thus, we performed a multi-year spin-up using the community Noah-MP column model within the high-resolution land data assimilation system (HRLDAS) modeling framework (Chen et al., 2007), which was forced by site-level FLUXNET meteorological observations. The model was initialized by repeatedly cycling through a complete 1-year forcing dataset ten consecutive times, resulting

https://doi.org/10.5194/egusphere-2026-4875
Preprint. Discussion started: 21 September 2026

Table 1. List of FLUXNET sites over which the model was evaluated. Vegetation, soil type, and Köppen climate classification are shown along with the simulation time period. Leaf area index, vegetation canopy height, and forcing tower height are also provided. Vegetation type: DBF- Deciduous broadleaf forest, ENF- Evergreen needleleaf forest, EBF- Evergreen broadleaf forest. Köppen classification: Dfb - Snow fully humid warm summer, Cfb - Warm temperate fully humid with warm summer, Csb - Warm temperate with dry, warm summer, Cfa - Warm temperate fully humid with hot summer, Cfb - Warm temperate fully humid with warm summer. Number of data points: US-UMB (Gough et al., 2015) = 1153, DE-HAI (Knohl et al., 2016) = 1290, US-Me2 (Law, 2016) = 2953, US-MMS (Novick and Phillips, 2016) = 791 and AU-Tum (Woodgate et al., 2016) = 655.

Site	Vegetation type	Soil type	Köppen classification	Time period	Leaf area index ($m^2\,m^{-2}$)	Canopy height (m)	Tower height (m)
US-UMB	DBF	Sand	Dfb	Aug–Sept 2017	4.2	21	46
DE-HAI	DBF	Clay loam	Cfb	Sept–Oct 2005	4.5	34	44
US-Me2	ENF	Sandy loam	Csb	Apr–Aug 2009	3.8	18	33
US-MMS	DBF	Silt loam	Cfa	Jul–Aug 2005	4.7	27	46
AU-Tum	EBF	Sandy clay loam	Cfb	Apr–May 2011	4.5	41	70

Table 2. Experiments were conducted using the community Noah-MP model, the community Noah-MP model with new parameterizations, and the Noah-MP-ML^2 model. MOST: Monin-Obukhov Similarity theory, H&F RSL: Harman and Finnigan roughness sublayer theory.

Experiments	Canopy type	Radiation	Stomatal conductance	Turbulence	Richards solver
Community Noah-MP	Single-layer	gap probability	Ball-Berry	MOST	Default Noah-MP
Noah-MP Medlyn	Single-layer	gap probability	Medlyn	MOST	Default Noah-MP
Noah-MP RSL	Single-layer	gap probability	Ball-Berry	H&F RSL	Default Noah-MP
Noah-MP Medlyn + RSL	Single-layer	gap probability	Medlyn	H&F RSL	Default Noah-MP
Noah-MP-ML^2 4 sub–surface layers	Multi-layer	SPARTACUS	Medlyn	H&F RSL	Default Noah-MP
Noah-MP-ML^2 20 sub–surface layers	Multi-layer	SPARTACUS	Medlyn	H&F RSL	Detailed solver

in a 10-year effective spin-up. This procedure allowed the deeper soil layers to equilibrate. After the final spin-up cycle, the simulated $\theta_{\rm liq}$ and soil temperature profiles were extracted and interpolated on the soil grids.

6.1 Experiments

We conducted six experiments with increasing complexity to evaluate Noah-MP-ML^2. These experiments are shown in Table 2. The detailed model set-up parameters for all the experiments are provided in Appendix B.

Community Noah-MP: Noah-MP v5.0 was implemented as a column model within HRLDAS. Radiative transfer is calculated using a 2-stream approximation with a Θ_z dependent gap probability. Stomatal conductance follows the Ball–Berry formula-

https://doi.org/10.5194/egusphere-2026-4875
Preprint. Discussion started: 21 September 2026

tion, and MOST was applied over vegetated and bare surface fractions separately. Soil water diffusion was solved using the default Noah-MP Richards equation solver with a free drainage lower boundary condition, while surface infiltration and runoff were parameterized using the Schaake scheme.

Noah-MP Medlyn: Same as the community Noah-MP configuration, but the Medlyn stomatal conductance model was used instead of Ball-Berry.

Noah-MP RSL: Same as the community Noah-MP configuration, but the single-layer Harman-Finnigan RSL scheme implemented by Abolafia-Rosenzweig et al. (2021) was used instead of MOST.

Noah-MP Medlyn + RSL: Same as the community Noah-MP configuration, but uses Medlyn stomatal conductance model and the single-layer RSL scheme for turbulence.

Noah-MP-ML^2 4 sub–surface layers: Uses SPARTACUS radiation transfer model, Medlyn stomatal conductance model, and Harman-Finnigan RSL scheme for turbulence, all implemented in a multilayer configuration as discussed in the paper. The model, however, uses the community Noah-MP 4-layer sub-surface grid and the default Noah-MP Richards equation solver.

Noah-MP-ML^2 20 sub–surface layers: Same as the Noah-MP-ML2 4-layer sub-surface model but uses the detailed Richards solver with van Genuchten water retention curves, solved on the 20-layer stretched soil grid.

6.2 Validation

We compared the net radiation, sensible heat flux, latent heat flux, friction velocity, and soil moisture and soil temperature profiles for all six experiments against the observations. This section only discusses the behavior of the model experiments in simulating these variables and the explanation for the observed behavior is presented later in Section 7.

6.2.1 Canopy variables

To provide an integrated assessment of model performance across sites and variables, we quantified the model skill for simulating net radiation, friction velocity, and turbulent heat fluxes using the Taylor skill score (Taylor, 2001). The Taylor score is a value between 0 and 1, where values closer to unity indicate higher agreement with observations. Table 3 provides the average Taylor skill scores for all the experiments at the selected sites. The Taylor diagrams for individual sites are provided in Figures S1 to S5 in the supplementary material.

Additionally, hourly data over the time period of the simulation were aggregated to study the diurnal profiles of variables for all the experiments. Figure 8 shows the diurnal profile for the US-UMB station along with the root mean squared error (RMSE) and mean bias for the entire time period of simulation. These metrics quantify the overall model error and systematic bias, respectively, which are not fully captured by the Taylor scores. Similar Figures for all the stations are provided in Figures S6 to S9 in the supplementary material.

Results from Table 3 show that the simulation of u_* consistently improved across most sites for the multilayer model experiments with the RSL parameterization when compared to the community Noah-MP model. The RSL implementation within the single-layer configuration only showed improved skill over the US-Me2 and AU-Tum sites. Site-specific analyses indicate that although the single-layer RSL formulation reduced nighttime underestimation of u_*, daytime values were often lower

https://doi.org/10.5194/egusphere-2026-4875
Preprint. Discussion started: 21 September 2026

Table 3. Average Taylor skill scores for the net radiation, friction velocity (u_*), and turbulent heat fluxes for all the experiments across the validation sites selected. The community Noah-MP model is used as a benchmark (italics), and all the model experiments that outperformed the community Noah-MP model are shown in bold.

	Experiments	US-UMB	DE-HAI	US-Me2	US-MMS	AU-Tum
Net Radiation	*Community Noah-MP*	*0.99*	*0.99*	*0.99*	*0.99*	*0.98*
	Noah-MP Medlyn	**0.99**	**0.99**	0.99	**0.99**	**0.98**
	Noah-MP RSL	**0.99**	**0.99**	0.99	**0.99**	**0.99**
	Noah-MP Medlyn + RSL	**0.99**	**0.99**	0.99	**0.99**	**0.99**
	Noah-MP-ML^2 4 sub–surface layers	**0.99**	**0.99**	0.99	**0.99**	**0.98**
	Noah-MP-ML^2 20 sub–surface layers	**0.99**	**0.99**	0.99	**0.99**	**0.98**
u_*	*Community Noah-MP*	*0.61*	*0.48*	*0.56*	*0.58*	*0.23*
	Noah-MP Medlyn	0.61	0.48	0.56	0.57	0.23
	Noah-MP RSL	0.46	0.45	**0.63**	0.20	**0.28**
	Noah-MP Medlyn + RSL	0.45	0.41	**0.61**	0.19	**0.27**
	Noah-MP-ML^2 4 sub–surface layers	**0.79**	**0.84**	**0.83**	**0.59**	**0.63**
	Noah-MP-ML^2 20 sub–surface layers	**0.79**	**0.83**	**0.83**	**0.58**	**0.63**
Sensible heat flux	*Community Noah-MP*	*0.70*	*0.87*	*0.86*	*0.51*	*0.69*
	Noah-MP Medlyn	**0.80**	0.86	0.83	**0.59**	**0.77**
	Noah-MP RSL	0.60	0.73	0.81	0.33	0.54
	Noah-MP Medlyn + RSL	0.67	0.71	0.81	0.37	0.59
	Noah-MP-ML^2 4 sub–surface layers	**0.84**	0.59	0.85	**0.56**	0.60
	Noah-MP-ML^2 20 sub–surface layers	**0.75**	0.63	**0.90**	**0.54**	0.64
Latent heat flux	*Community Noah-MP*	*0.75*	*0.72*	*0.56*	*0.89*	*0.59*
	Noah-MP Medlyn	**0.88**	**0.86**	**0.69**	**0.89**	**0.72**
	Noah-MP RSL	0.67	0.69	0.49	0.85	0.57
	Noah-MP Medlyn + RSL	**0.81**	**0.78**	**0.66**	0.86	**0.71**
	Noah-MP-ML^2 4 sub–surface layers	0.74	**0.82**	**0.76**	0.85	**0.68**
	Noah-MP-ML^2 20 sub–surface layers	0.71	**0.83**	**0.65**	0.83	**0.71**

than those simulated using MOST-based formulations (e.g., Figure 8 for US-UMB and supplementary section S2). Additional stability-dependent diagnostics are required to better understand this behavior and to further evaluate the performance of the RSL parameterization within both single-layer and multilayer configurations.

Overall, all experiments show good agreement in the simulation of net radiation. The Taylor scores remained consistently high across sites. However, the use of SPARTACUS provides a physically consistent multiband solution to the canopy radiative transfer in both shortwave and longwave spectral bands.

Across the five sites, the Taylor scores for sensible heat flux varied over a wide range, similar to u_*, indicating strong sensitivity to the canopy turbulence formulations. The highest skill for sensible heat flux was observed at US-Me2 and DE-HAI, where the multilayer configurations reached scores up to 0.9. In contrast, US-MMS represented a more challenging

https://doi.org/10.5194/egusphere-2026-4875
Preprint. Discussion started: 21 September 2026

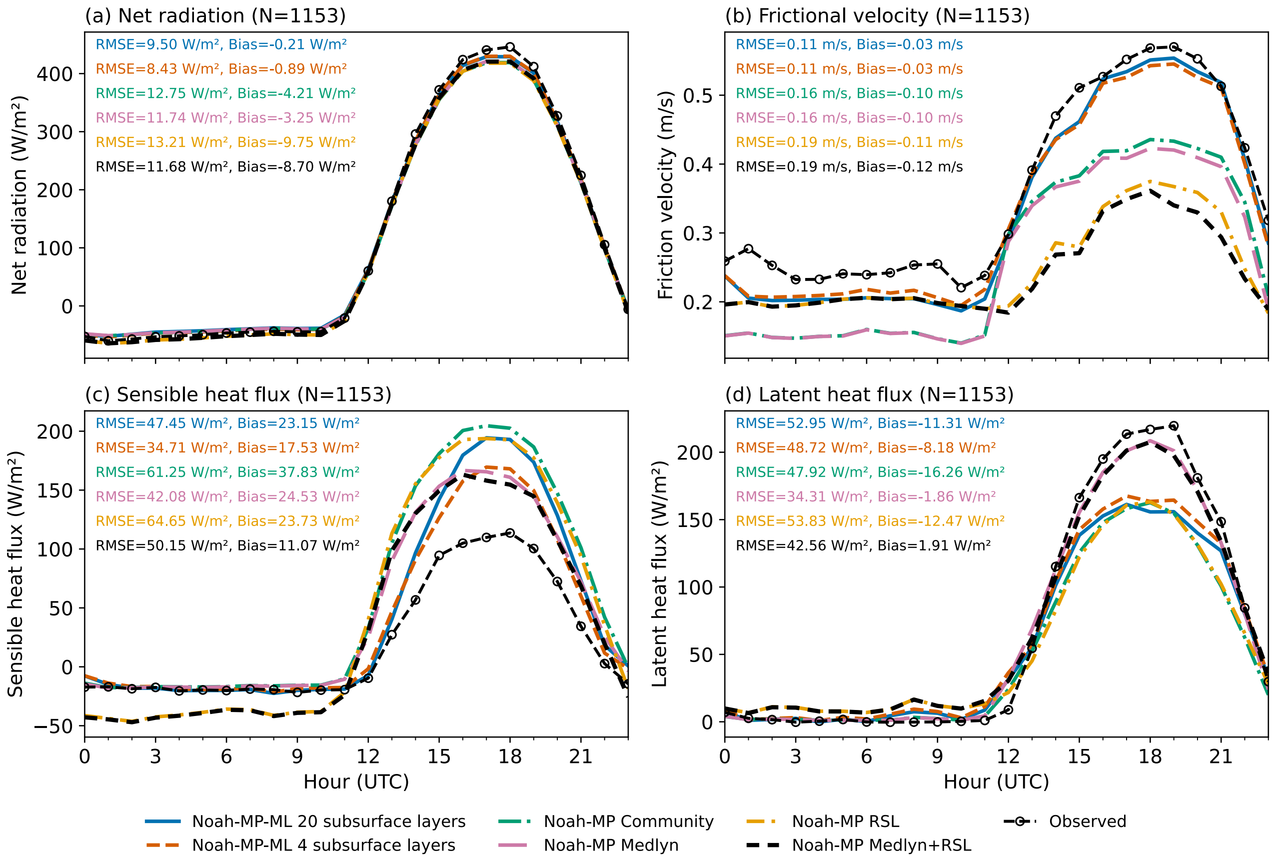

Figure 8. Averaged diurnal profiles of net radiation, friction velocity, sensible heat flux, and latent heat flux for all the experiments at the US-UMB FLUXNET station. RMSE and bias are also shown for different experiments.

site. US-UMB and AU-Tum show moderate to good performance depending on the configuration. Among all experiments, the Noah-MP Medlyn experiment provided consistently strong results across sites. The multilayer configurations also perform well. The single-layer RSL implementations generally reduced the sensible heat flux skill at several sites, most prominently at US-MMS. This reduction in performance was due to a consistent large negative nighttime sensible heat flux predicted by the single-layer RSL implementation (e.g., Figure 8 for US-UMB and supplementary section S2). Despite these differences, all experiments broadly captured the timing of the daytime peak in sensible heat flux, while disagreements arose primarily in peak magnitude and nighttime behavior.

For latent heat flux, Taylor scores were generally higher and less variable than those of sensible heat flux. US-MMS was the most skillful site across all experiments, while US-UMB and DE-HAI also showed good overall performance. In contrast, US-Me2 and AU-Tum were more challenging sites for latent heat flux simulation. The Noah-MP Medlyn experiment again demonstrated a robust performance across sites. The multilayer experiments are generally competitive, especially at DE-HAI

https://doi.org/10.5194/egusphere-2026-4875
Preprint. Discussion started: 21 September 2026

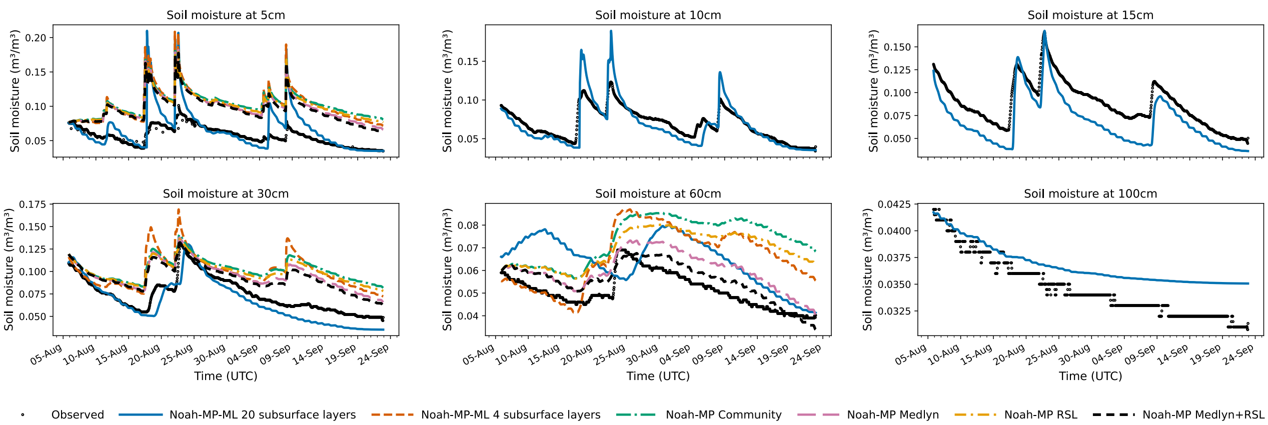

Figure 9. Soil liquid water (in this case equals the volumetric soil moisture) simulation at different depths for various experiments conducted at the US-UMB FLUXNET station.

and US-MMS. The single-layer RSL experiment showed a degraded performance that was partially mitigated when combined with the Medlyn stomatal conductance scheme. The diurnal profiles of latent heat flux showed behavior similar to those of sensible heat flux: all experiments reproduced the diurnal profile, but the differences emerged in the magnitude of the daytime peak. Lastly, the RSL experiments showed a non-negligible nighttime latent heat flux even when observations are close to zero (e.g., Figure 8 for US-UMB and supplementary section S2).

6.2.2 Sub-surface variables

RMSE, bias, and correlation coefficient (R) were used to evaluate soil temperature and soil moisture simulations across all model experiments and sites. Because the exact measurement depths do not always coincide with the midpoints of model soil layers, the nearest model grid midpoint available to each observed depth was used for comparison. The standard 4-layer community Noah-MP sub-surface column corresponds to midpoint depths of 5, 25, 70, and 150 cm. In contrast, the 20-layer sub-surface configuration employs a finer vertical discretization (see Table A1 in appendix). This allowed more observed depths to align with the modeled midpoints. Figures 9 and 10 further show the simulated soil moisture and soil temperature for the six experiments at the US-UMB site. Such plots at other sites are provided in sections S3 and S4 in the supplementary material.

Proper representation of near-surface soil moisture is important because a large fraction of the root biomass is concentrated within these layers (Jackson et al., 1996), which directly impacts the soil moisture stress to transpiration. Thus, Table 4 summarizes the evaluation metrics for soil moisture and soil temperature for the topmost observational depth at all sites. For completeness, the full set of evaluation metrics across all available depths is provided in section S5 of the supplementary material.

At US-UMB and DE-HAI, the multilayer model with 20 sub-surface layers showed reduced RMSE and bias for soil moisture compared to the community Noah-MP experiments. The Medlyn experiments also provided moderate improvements relative

https://doi.org/10.5194/egusphere-2026-4875
Preprint. Discussion started: 21 September 2026

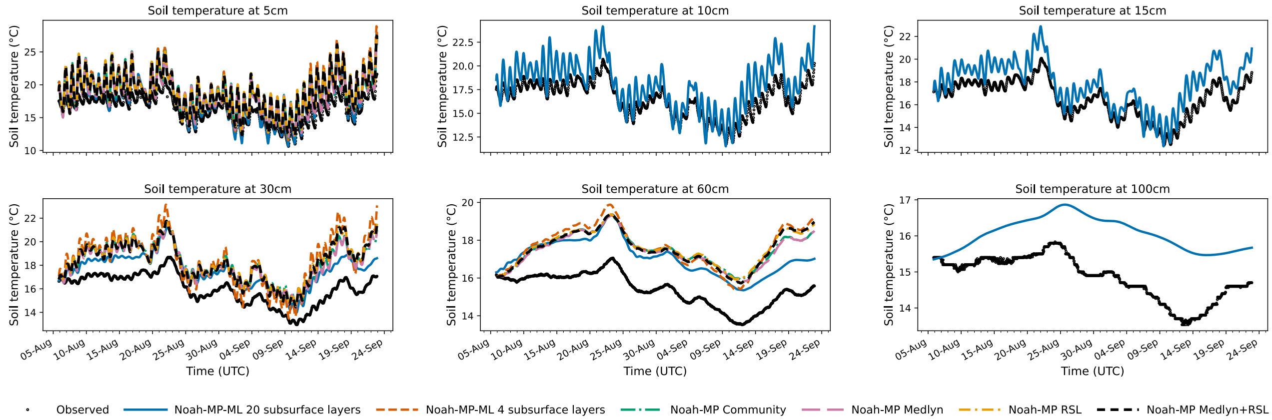

Figure 10. Soil temperature simulation at different depths for various experiments conducted at the US-UMB FLUXNET station.

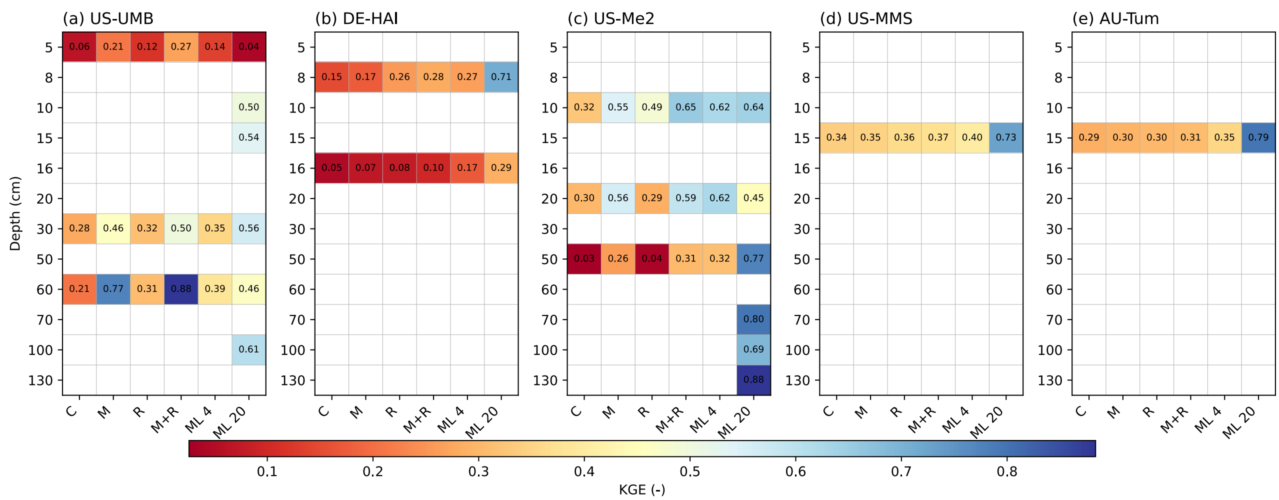

Figure 11. Kling–Gupta efficiency (KGE) of simulated soil moisture across the five study sites and available observational depths. Model performance is evaluated using the subsurface layer whose midpoint depth is closest to the corresponding observation level. C: Community Noah-MP, M: Noah-MP Medlyn, R: Noah-MP RSL, M+R: Noah-MP Medlyn+RSL, ML4: Noah-MP-ML^2 4 sub–surface layers, and ML20: Noah-MP-ML^2 20 sub–surface layers.

to the community Noah-MP experiment. Soil temperature simulations exhibited consistently high correlations across all experiments, indicating that the temporal variability is generally well captured. But the differences primarily arose from the magnitude. To provide a more integrated assessment that combines variability, correlation, and bias into a single diagnostic metric, Figure 11 shows the Kling–Gupta Efficiency (KGE) (Gupta et al., 2009) for soil moisture at different observational depths for the sites selected.

https://doi.org/10.5194/egusphere-2026-4875
Preprint. Discussion started: 21 September 2026

Table 4. Validation of observed top-layer soil moisture and temperature against observations. Note that the nearest subsurface midpoint was used for comparison. Also note that for US-MMS and AU-Tum, the soil moisture and temperature were measured at different depths. US-MMS: 15 cm and 5 cm, and AU-Tum: 15 cm and 2 cm. The community Noah-MP model is used as a benchmark (italics), and all the model experiments that outperformed the community Noah-MP model are shown in bold.

Site and depth	Model experiment	Soil moisture RMSE ($m^3\,m^{-3}$)	Soil moisture Bias ($m^3\,m^{-3}$)	Soil moisture R	Soil temperature RMSE (K)	Soil temperature Bias (K)	Soil temperature R
US-UMB 5 cm	*Community Noah-MP*	*0.05*	*0.05*	*0.62*	*2.74*	*2.40*	*0.90*
	Noah-MP Medlyn	**0.04**	**0.04**	**0.71**	**2.65**	**2.30**	**0.90**
	Noah-MP RSL	**0.05**	**0.04**	**0.65**	2.93	2.59	0.89
	Noah-MP Medlyn + RSL	**0.04**	**0.04**	**0.74**	2.84	2.50	**0.90**
	Noah-MP-ML^2 4 sub–surface layers	**0.05**	**0.04**	**0.63**	2.91	2.53	**0.92**
	Noah-MP-ML^2 20 sub–surface layers	**0.02**	**0.01**	**0.72**	**2.48**	**2.01**	**0.93**
DE-HAI 8 cm	*Community Noah-MP*	*0.09*	*0.09*	*0.56*	*1.06*	*-0.19*	*0.98*
	Noah-MP Medlyn	**0.09**	**0.08**	**0.60**	1.06	-0.28	**0.98**
	Noah-MP RSL	**0.08**	**0.08**	**0.63**	**0.81**	**-0.12**	**0.99**
	Noah-MP Medlyn + RSL	**0.08**	**0.07**	**0.67**	**0.80**	**-0.14**	**0.99**
	Noah-MP-ML^2 4 sub–surface layers	**0.08**	**0.07**	**0.73**	**0.87**	-0.36	**0.99**
	Noah-MP-ML^2 20 sub–surface layers	**0.03**	**0.02**	**0.74**	**0.69**	**0.06**	**0.99**
US-Me2 10 cm	*Community Noah-MP*	*0.08*	*0.07*	*0.94*	*4.77*	*-2.26*	*0.85*
	Noah-MP Medlyn	**0.06**	**0.05**	**0.97**	**4.74**	**-2.18**	0.85
	Noah-MP RSL	**0.06**	**0.06**	**0.95**	**4.41**	**-0.37**	0.83
	Noah-MP Medlyn + RSL	**0.05**	**0.04**	**0.98**	**4.51**	**-0.43**	0.82
	Noah-MP-ML^2 4 sub–surface layers	**0.05**	**0.04**	**0.97**	**4.41**	**-1.31**	0.84
	Noah-MP-ML^2 20 sub–surface layers	**0.04**	**-0.02**	0.91	5.36	**-1.49**	0.75
US-MMS 15 and 5 cm	*Community Noah-MP*	*0.03*	*-0.01*	*0.93*	*4.90*	*4.64*	*0.81*
	Noah-MP Medlyn	0.04	-0.01	0.91	**4.81**	**4.55**	**0.81**
	Noah-MP RSL	0.04	-0.02	0.90	**3.50**	**3.24**	**0.84**
	Noah-MP Medlyn + RSL	0.04	-0.02	0.86	**3.50**	**3.24**	**0.84**
	Noah-MP-ML^2 4 sub–surface layers	0.04	-0.02	0.88	**3.85**	**3.58**	**0.81**
	Noah-MP-ML^2 20 sub–surface layers	0.05	-0.04	0.77	**4.27**	**3.91**	0.69
AU-Tum 15 cm and 2 cm	*Community Noah-MP*	*0.05*	*0.05*	*0.96*	*1.56*	*-1.16*	*0.87*
	Noah-MP Medlyn	**0.05**	**0.05**	0.96	1.59	-1.22	**0.87**
	Noah-MP RSL	**0.05**	**0.04**	0.95	**1.32**	**-0.74**	0.79
	Noah-MP Medlyn + RSL	**0.05**	**0.04**	0.94	**1.32**	**-0.77**	0.79
	Noah-MP-ML^2 4 sub–surface layers	**0.04**	**0.04**	0.94	**1.47**	**-1.10**	0.86
	Noah-MP-ML^2 20 sub–surface layers	**0.02**	**0.02**	0.88	1.80	**-0.89**	0.73

The 20-layer sub-surface model simulations maintain comparatively strong performance across all depths. The single-layer Medlyn experiments also showed increased skill with depth compared to the community Noah-MP model.

https://doi.org/10.5194/egusphere-2026-4875
Preprint. Discussion started: 21 September 2026

7 Discussion

A consistent improvement in the simulation of u_* with the multilayer canopy model is noticed across all sites (Table 3). This finding is consistent with Bonan et al. (2018) and the behavior is expected because the vertical gradients of momentum within and immediately above vegetated canopies deviate from the assumptions of MOST, and the Harman-Finnigan RSL scheme accounts for these departures through modified stability functions in the roughness sublayer. These results further suggest that the representation of momentum exchange over tall forests benefits from the inclusion of RSL physics within the multilayer configuration. The differences between the single-layer and multilayer RSL u_* results arise due to a subtle implementation detail; in the multilayer canopy configuration, the RSL correction is applied during the iterative solution for the Obukhov length and u_*, while the single layer implementation modifies the integrated form of momentum and scalar stability RSL functions, which is then used to calculate u_* and aerodynamic resistance between the reference height and the effective canopy surface.

For the sites tested, the community Noah-MP model tends to shift the energy partitioning toward sensible heat flux at the expense of latent heat flux, but implementing the Medlyn stomatal conductance model led to consistent improvements in the turbulent heat flux prediction skill. This is because of the stomatal conductance-VPD relationship in the Medlyn formulation that predicts a higher stomatal conductance value (and transpiration) for a given VPD compared to the Ball-Berry model for the Medlyn parameters used in this study. The differences in latent heat flux among experiments that used the Medlyn stomatal conductance model (Noah-MP Medlyn, Noah-MP Medlyn+RSL, Noah-MP-ML^2 4-layers sub-surface and Noah-MP-ML^2 20-layers sub-surface) are explained below. The results for sensible heat flux are somewhat complementary to latent heat flux as different model configurations did not have a significant impact on the ground heat flux.

Canopy humidity constraint and stomatal conductance implementation method: In the community Noah-MP Ball–Berry stomatal conductance model implementation, the canopy air vapor pressure used for the stomatal closure is constrained such that the canopy relative humidity does not fall below $25\,\%$ of saturation for C_3 vegetation and $40\,\%$ for C_4 vegetation (a numerical stability safeguard). The same constraint was retained in the Noah-MP Medlyn and Noah-MP Medlyn+RSL experiments for consistency. However, in the Noah-MP-ML^2 configurations, this constraint is not used as this implementation followed Bonan et al. (2018). As a result, the Noah-MP Medlyn and Noah-MP Medlyn+RSL experiments effectively limit high VPD stress. Thus, these experiments can sustain higher stomatal conductance under dry canopy conditions compared to the multilayer model simulations. Further, the Noah-MP Medlyn and Noah-MP Medlyn+RSL experiments use 3 iterations by default to compute the intercellular CO_2 to satisfy the gross carbon assimilation, while the Noah-MP-ML^2 configurations continue the iteration until the CO_2 diffusivity constraint is met for net carbon assimilation. These points mainly explain the differences in latent heat flux simulations for Noah-MP Medlyn and Noah-MP-ML^2 4-layer sub-surface model (same sub-surface grid and the default Noah-MP Richards equation solver used in these experiments).

Influence of soil water dynamics and soil moisture stress: To understand why Noah-MP Medlyn implementation mostly outperformed the Noah-MP-ML^2 20-layer sub-surface model, we need to examine vadose-zone hydrological representation in both these configurations. The partitioning of turbulent heat fluxes is also controlled by θ_{liq}: when sufficient soil water is

https://doi.org/10.5194/egusphere-2026-4875
Preprint. Discussion started: 21 September 2026

available, a larger fraction of the absorbed net radiation is partitioned to latent heat flux. Consequently, the representation of the soil water column plays a critical role in land–atmosphere coupling. In the community Noah-MP configuration (and all 4-layer sub-surface layer experiments), the soil moisture stress to transpiration is calculated by aggregating a layer-wise wetness factor using layer thickness as the weighting factor for all the rooting layers. In contrast, in the 20-layer sub-surface model, the wetness factor is aggregated using a root fraction weighting, where root distributions follow Jackson et al. (1996) root profiles. This means that the layers containing more root fraction exert a stronger control on the soil moisture stress in the 20-layer sub-surface model. Because root fractions are concentrated toward the near-surface in the 20-layer sub-surface model, it places greater emphasis on upper soil layers, and also the Richards solver used in the 20-layer sub-surface model produces drier top soil layers. As a result, the 20-layer sub-surface model tends to produce a stronger transpiration limitation under dry conditions compared to the 4-layer sub-surface model. Another important contributing factor is that the default 4-layer sub-surface Noah-MP Richards equation solver tends to retain water within the soil column (likely due to soil hydraulic properties, parameter calibration or solution method) as evident in the soil moisture time series plots (Figure 9 and section S3 in the supplementary material). This further reduces the soil moisture stress in all the 4-layer sub-surface model experiments.

In all the 4-layer sub-surface experiments, infiltration is parameterized using the Schaake scheme, and the θ_{liq} form of the Richards equation is used to calculate the water diffusion within the soil column, where the soil hydraulic properties are calculated based on the θ_{liq} from the previous time step (no iterative solution). This formulation is numerically robust and is unconditionally stable under most conditions. In contrast, solving the full Richards equation in the 20-layer sub-surface model introduces additional numerical complexity due to iterative solution, and the convergence is not always guaranteed. The use of van Genuchten soil water retention curves introduces additional uncertainty, as it is difficult to obtain these parameters for different soil types. Although datasets such as Carsel and Parrish (1988) provide representative parameter values for common soil textures, site-specific properties may deviate substantially from these standard values (Chavoshi et al., 2025).

At the US-UMB site, the turbulent heat flux partitioning illustrates how a more process-explicit representation of soil–plant–atmosphere interactions can reveal potential compensating errors. When the baseline Carsel and Parrish (1988) parameters were used, rapid drainage from the coarse-textured soil produced dry upper layers and strong soil-moisture stress, ultimately shifting the simulated energy partitioning toward sensible heat flux. Reducing the saturated hydraulic conductivity improved the simulated soil-moisture profiles at US-UMB, although this adjustment should be regarded as site-specific parameter calibration. Previous studies have similarly characterized US-UMB as a xeric site and shown that canopy water use depends on water availability throughout the active root zone (Frasson et al., 2015; Matheny et al., 2014). The remaining discrepancies may therefore reflect uncertainty in the prescribed soil hydraulic properties and root distribution, as well as plant hydraulic processes that are not currently represented in Noah-MP-ML^2. Incorporating an explicit plant-hydraulics scheme, such as that developed for Noah-MP by Li et al. (2021), may improve the representation of soil-water uptake and turbulent heat flux partitioning at sites such as US-UMB.

All simulations assumed a fully mineral soil profile without organic matter. Because soil organic matter modifies the hydraulic and thermal properties governing soil-water and heat diffusion (Lin et al., 2026), this assumption introduces additional

https://doi.org/10.5194/egusphere-2026-4875
Preprint. Discussion started: 21 September 2026

uncertainty. The limitation may be particularly relevant at US-UMB, where litter and organic material strongly influence the shallow soil layers.

Lastly, we found that the prediction skill for soil moisture at different depths improved in the 4-layer sub-surface Noah-MP Medlyn experiment compared to the community Noah-MP model. This is again related to the higher transpiration rate with the Medlyn model, which means that there is a higher root water uptake.

8 Conclusions

The comparison of model experiments demonstrates that land–atmosphere exchange and subsurface states are jointly influenced by canopy physiology, radiative transfer, aerodynamic representation, and subsurface hydrology. The Taylor skill scores show that the Medlyn-based experiments generally improved latent heat flux performance while maintaining good sensible heat flux skill. The multilayer implementation of the RSL parameterization improved friction velocity skill at four sites and maintained performance comparable to community Noah-MP at US-MMS. Compared with the single-layer Medlyn+RSL experiment, the multilayer configuration generally improved or maintained sensible heat flux skill, except at DE-HAI. Latent heat flux skill improved at DE-HAI, remained comparable at US-Me2 and AU-Tum, declined slightly at US-MMS, and declined more substantially at US-UMB. The KGE results indicate that the 20-layer subsurface model with the detailed Richards solver generally improved the representation of vertical soil-moisture dynamics at many of the evaluated sites and depths, although its performance remained sensitive to the prescribed hydraulic parameters. Future work should investigate site-specific van Genuchten parameters, organic-soil properties, root distributions, and plant hydraulics.

Code and data availability. The version of Noah-MP-ML^2 used in this study (v1.0), including the source code, user manual, model configuration, and example forcing data, is archived at Zenodo: https://doi.org/10.5281/zenodo.21908465, (Kamath et al., 2026). The version of community Noah-MP model used in our study can also be found on Zenodo: https://doi.org/10.5281/zenodo.7901854, He et al. (2023a). The FLUXNET datasets used in this study can be found here - US-UMB: https://doi.org/10.18140/FLX/1440093, (Gough et al., 2015); DE-HAI: https://doi.org/10.18140/FLX/1440148, (Knohl et al., 2016); US-Me2: https://doi.org/10.18140/FLX/1440079, (Law, 2016); US-MMS: https://doi.org/10.18140/FLX/1440083, (Novick and Phillips, 2016); AU-Tum: https://doi.org/10.18140/FLX/1440126, (Woodgate et al., 2016).

Appendix A: Sub-surface setup

The sub-surface is set-up as non-uniform, vertically stretched grid with shallow layers near the top as discussed in the main text. The soil properties and scalars like the volumetric liquid water content, matric potential, hydraulic conductivity, etc., are on the grid midpoints as shown in Figure A1. In the present case, we used the thickness of the first layer to be 1 cm and a 20-layer grid going up to 2 meters deep. The resulting layer thickness, cumulative depths and grid midpoint depths are presented in Table A1.

https://doi.org/10.5194/egusphere-2026-4875
Preprint. Discussion started: 21 September 2026

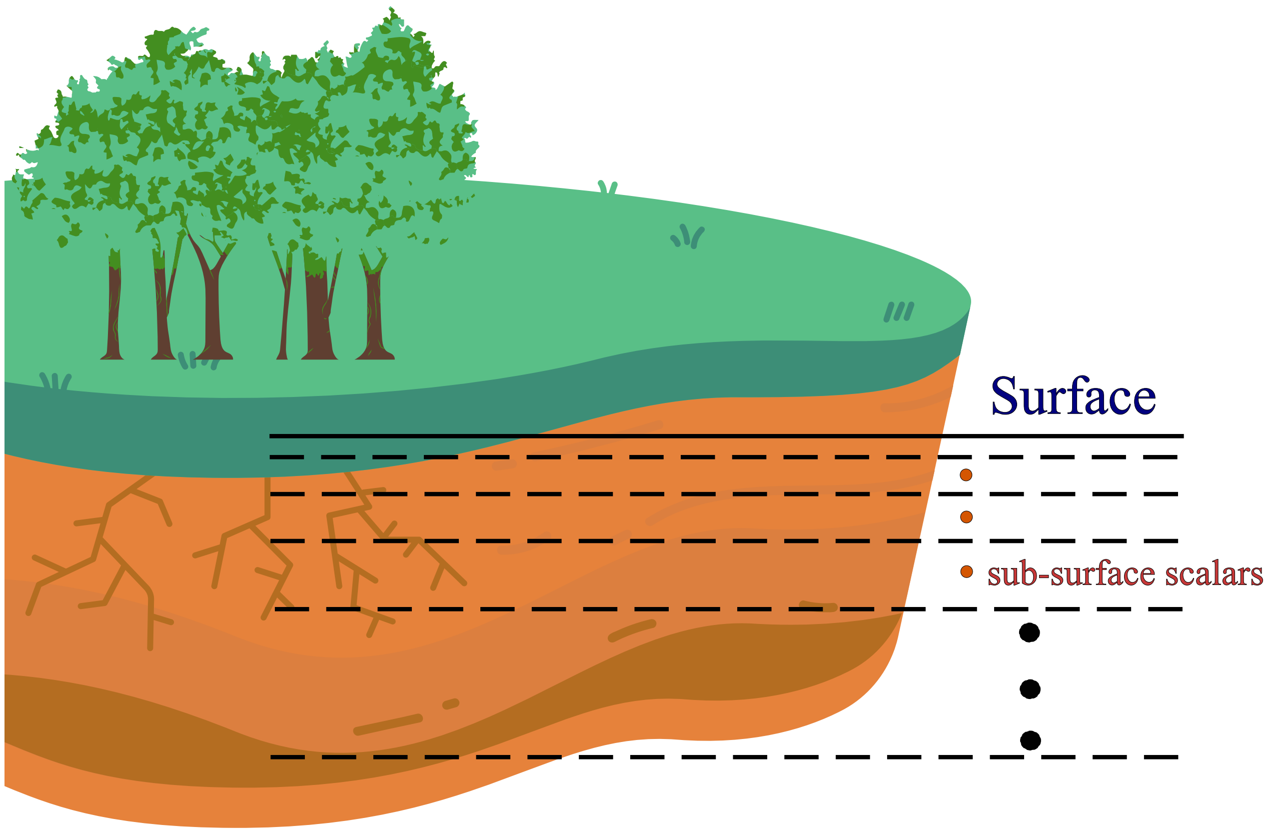

Figure A1. Illustration of sub-surface grid setup.

Appendix B: Detailed experiment set-up information

All the single-layer Noah-MP experiments shown in Table 2 of the main text were conducted as column models implemented using the HRLDAS framework (Chen et al., 2007). The canopy and surface properties of these experiments were fetched from the Noah-MP look-up table. Important community Noah-MP namelist options other than ones mentioned in Table 2 of the main text are: (i) fully implicit soil temperature solver and time sub-step of 10 minutes within the hourly forcing interval. For the SPARTACUS radiation transfer model, the namelist options used are provided in Table B1.

The properties of the canopy used for the multilayer model for the forest types simulated is shown in Table B2. For the ground radiative properties, the emissivity was set to 0.96 and, the albedo was 0.18 and 0.36 in visible and NIR spectral bands, respectively.

To simulate the sub-surface, soil properties are required. When the community Noah-MP model is run using HRLDAS, the values are taken from the Noah-MP look-up table (Clapp and Hornberger, 1978). When the 20-layer sub-surface model is used, important soil properties that are summarized in Table B3 are used. The van Genuchten (van Genuchten, 1980) properties are

https://doi.org/10.5194/egusphere-2026-4875
Preprint. Discussion started: 21 September 2026

Table A1. Thickness, cumulative depths, and midpoint depths of the 20-layer stretched grid used in our study.

Layer	Thickness (cm)	Cumulative depth (cm)	Midpoint depth (cm)
1	1	1	0.5
2	1.2	2.2	1.6
3	1.5	3.7	2.95
4	1.8	5.5	4.6
5	2.1	7.6	6.55
6	2.5	10.1	8.85
7	3.1	13.2	11.65
8	3.7	16.9	15.05
9	4.5	21.4	19.15
10	5.4	26.8	24.1
11	6.5	33.3	30.05
12	7.8	41.1	37.2
13	9.4	50.5	45.8
14	11.4	61.9	56.2
15	13.7	75.6	68.75
16	16.5	92.1	83.85
17	19.9	112	102.05
18	24	136	124
19	29	165	150.5
20	34.9	200	182.45

Table B1. Namelist options for the SPARTACUS radiation transfer model.

SPARTACUS	
Number of regions	3
Solution type	2-stream
Number of shortwave bands	2 (visible and NIR)
Number of longwave bands	1
Number of bands in the visible	1 (PAR)
Canopy set-up	
Vertical resolution of the canopy	50 cm

https://doi.org/10.5194/egusphere-2026-4875
Preprint. Discussion started: 21 September 2026

Table B2. Canopy, leaf geometry, and radiative, stomatal conductance, and photosynthesis properties for: DBF- Deciduous broadleaf forest, ENF- Evergreen needleleaf forest, EBF- Evergreen broadleaf forest.

	DBF	ENF	EBF
Canopy structure and leaf geometry			
Beta distribution p-parameter $(-)$	3.5	3.5	3.5
Beta distribution q-parameter $(-)$	2	2	2
Specific leaf area ($\mathrm{m^2\,g^{-1}\,C}$)	0.03	0.008	0.012
Leaf dimensional length (m)	0.04	0.04	0.04
Leaf angle departure $(-)$	0.25	0.01	0.1
Photosynthesis and stomatal conductance			
Photosynthetic pathway $(-)$	C_3	C_3	C_3
Maximum carboxylation rate at 25 °C ($\mathrm{\mu mol\,m^{-2}\,s^{-1}}$)	57.7	62.5	61.4
Medlyn minimum conductance ($\mathrm{mol\,m^{-2}\,s^{-1}}$)	0.0001	0.0001	0.0001
Medlyn slope ($\mathrm{kPa^{1/2}}$)	4.45	2.35	4.12
Jackson beta $(-)$	0.98	0.98	0.966
Leaf radiative properties			
Leaf transmittance in visible $(-)$	0.05	0.05	0.05
Leaf transmittance in NIR $(-)$	0.25	0.1	0.25
Leaf reflectance in visible $(-)$	0.1	0.07	0.1
Leaf reflectance in NIR $(-)$	0.45	0.35	0.45
Leaf emissivity $(-)$	0.98	0.98	0.98

from Carsel and Parrish (1988). However, note that the residual soil moisture is reduced for some soils to match the minimum observed values. Further, the saturated hydraulic conductivity was reduced for coarser-textured soil as the water drained too fast compared to the observations.

https://doi.org/10.5194/egusphere-2026-4875
Preprint. Discussion started: 21 September 2026

Table B3. Soil properties for the 20-layer model. $\theta_{\mathrm{r,VG}}$: residual soil moisture, $\theta_{\mathrm{s,VG}}$: saturated soil moisture, α_{VG}: inverse air entry potential, n_{VG}: pore size distribution index and, $K_{\mathrm{VG,sat}}$: saturated hydraulic conductivity.

	Sand	Clay loam	Sandy loam	Silt loam	Sandy clay loam
Depth of soil for evaporation (cm)	10	10	10	10	10
Maximum pond depth (cm)	2	2	2	2	2
Soil heat capacity ($\mathrm{J\,m^{-3}\,K^{-1}}$)	2×10^6	2×10^6	2×10^6	2×10^6	2×10^6
Soil resistance parameter (−)	5	5	5	5	5
Soil quartz fraction (−)	0.92	0.35	0.6	0.25	0.6
van Genuchten parameters					
$\theta_{\mathrm{r,VG}}$ ($\mathrm{m^3\,m^{-3}}$)	0.03	0.095	0.05	0.067	0.1
$\theta_{\mathrm{s,VG}}$ ($\mathrm{m^3\,m^{-3}}$)	0.43	0.41	0.41	0.45	0.39
α_{VG} ($\mathrm{cm^{-1}}$)	0.145	0.019	0.075	0.02	0.059
n_{VG} (−)	2.68	1.31	1.89	1.41	1.48
$K_{\mathrm{VG,sat}}$ ($\mathrm{cm\,s^{-1}}$)	2.025×10^{-3}	7.22×10^{-5}	1.54×10^{-4}	1.25×10^{-4}	3.64×10^{-4}

https://doi.org/10.5194/egusphere-2026-4875
Preprint. Discussion started: 21 September 2026

Table C1. Generalized symbols for indices, photosynthesis, and stomatal conductance. Units are given in brackets.

Symbol	Description
i	Canopy or soil layer index $[-]$.
k	Shortwave spectral-band index $[-]$.
l	Longwave spectral-band index $[-]$.
p	Photosynthetically active radiation spectral-band index $[-]$.
n	Time-level index $[-]$.
m	Nonlinear iteration index $[-]$.
N	Number of discrete diffuse-radiation angles in each hemisphere $[-]$.
A_g	Gross CO_2 assimilation [μmol $\mathrm{m}^{-2}\,\mathrm{s}^{-1}$].
A_n	Net CO_2 assimilation [μmol $\mathrm{m}^{-2}\,\mathrm{s}^{-1}$].
c_s	CO_2 concentration at the leaf surface [μmol mol^{-1}].
c_i	Intercellular CO_2 concentration [Pa or μmol mol^{-1}, depending on the formulation].
$V_{c,\max}$	Maximum carboxylation rate [μmol $\mathrm{m}^{-2}\,\mathrm{s}^{-1}$].
β_soil	Soil-moisture-stress factor applied to photosynthesis $[-]$.
g^sw	Stomatal conductance for water vapor [$\mathrm{mol\,m}^{-2}\,\mathrm{s}^{-1}$].
g^sc	Stomatal conductance for CO_2 [$\mathrm{mol\,m}^{-2}\,\mathrm{s}^{-1}$].
g^bc	Leaf boundary-layer conductance for CO_2 [$\mathrm{mol\,m}^{-2}\,\mathrm{s}^{-1}$].
g_0^sw	Minimum Medlyn stomatal conductance [$\mathrm{mol\,m}^{-2}\,\mathrm{s}^{-1}$].
g_1^sw	Medlyn slope parameter [$\mathrm{kPa}^{1/2}$].
D_HC	Ratio of the diffusivity of H_2O to that of CO_2 $[-]$.
VPD	Vapor pressure deficit [kPa].
LAI_i	Leaf area index of canopy layer i [$\mathrm{m}^2\,\mathrm{m}^{-2}$].

Appendix C: Symbols and notation

The symbols used in the model are summarized below. Subscript i denotes a generalized canopy or soil layer; k, l, and p denote shortwave, longwave, and photosynthetically active radiation spectral bands, respectively; n denotes a time level; and m denotes a nonlinear iteration. The qualifiers $x = \mathrm{sun}, \mathrm{sha}$ distinguish sunlit and shaded foliage, and $y = \mathrm{veg}, \mathrm{bare}$ distinguish vegetated and bare surfaces.

https://doi.org/10.5194/egusphere-2026-4875
Preprint. Discussion started: 21 September 2026

Table C2. Generalized symbols for canopy and ground radiation. Units are given in brackets.

Symbol	Description
$\mathrm{Ext}_i^{\mathrm{dir/dif}}$	Volumetric extinction coefficient for direct or diffuse radiation in layer i [m^{-1}].
$G_{\mathrm{dir/dif}}$	Ross–Goudriaan leaf projection function for direct or diffuse radiation [$-$].
χ_l	Leaf-angle departure parameter [$-$].
ϕ_1, ϕ_2	Coefficients used in the Ross–Goudriaan leaf projection function [$-$].
Θ_z	Solar zenith angle [rad].
$S_k^{\mathrm{dir/dif}}$	Incident direct or diffuse shortwave radiation in spectral band k [$\mathrm{W\,m^{-2}}$].
$A_{i,k}^{\mathrm{dir/dif/tot}}$	Vegetation absorption in layer i per unit incident flux for direct, diffuse, or total radiation [$-$].
f_i^{sun}	Sunlit foliage fraction in canopy layer i [$-$].
$Q_{i,k}^x$	Layer-integrated shortwave absorption by sunlit or shaded foliage per unit ground area, $x = \mathrm{sun}, \mathrm{sha}$ [$\mathrm{W\,m^{-2}}$].
$q_{i,k}^{x,\mathrm{SW}}$	Absorbed shortwave radiation per unit leaf area for sunlit or shaded foliage [$\mathrm{W\,m^{-2}}$].
L_l^{sky}	Incident downwelling longwave radiation from the sky in spectral band l [$\mathrm{W\,m^{-2}}$].
$R_{i,l}^{\mathrm{emit}}$	Layer-integrated longwave absorption, including internal thermal emission, per unit ground area [$\mathrm{W\,m^{-2}}$].
$R_{i,l}^{\mathrm{abs}}$	Foliage absorption response to unit downwelling longwave forcing [$-$].
$q_{i,l}^{\mathrm{emit/abs,LW}}$	Longwave flux per unit leaf area due to internal emission or downwelling-radiation absorption [$\mathrm{W\,m^{-2}}$].
R_i^x	Net radiative flux per unit leaf area for sunlit or shaded foliage, $x = \mathrm{sun}, \mathrm{sha}$ [$\mathrm{W\,m^{-2}}$].
PAR_i^x	Photosynthetically active radiation for sunlit or shaded foliage [$\mathrm{\mu mol\,m^{-2}\,s^{-1}}$].
γ_p^{PAR}	Energy-to-photon conversion factor for PAR band p [$\mathrm{\mu mol\,J^{-1}}$].
$Q_{\mathrm{ground},k}^{\mathrm{dir/dif}}$	Ground shortwave-radiation response to unit direct or diffuse incident flux [$-$].
$R_{\mathrm{ground},l}^{\mathrm{emit}}$	Ground net longwave radiation due to internal thermal emission [$\mathrm{W\,m^{-2}}$].
$R_{\mathrm{ground},l}^{\mathrm{abs}}$	Ground absorption response to unit downwelling longwave forcing [$-$].
$Q_{\mathrm{ground}}^{\mathrm{SW/LW/net}}$	Ground shortwave, longwave, or total net radiation per unit ground area [$\mathrm{W\,m^{-2}}$].
α_{s}	Surface albedo [$-$].
c_{veg}	Fractional vegetation coverage [$-$].

https://doi.org/10.5194/egusphere-2026-4875
Preprint. Discussion started: 21 September 2026

Table C3. Generalized symbols for canopy turbulence. Units are given in brackets.

Symbol	Description
z_i	Height of canopy or atmospheric layer i above the ground [m].
h_c	Canopy height [m].
d^y	Displacement height for surface type $y = \text{veg}, \text{bare}$ [m].
L^y_{MO}	Obukhov length for surface type $y = \text{veg}, \text{bare}$ [m].
$z^y_{0\text{m}}$	Momentum roughness length for surface type $y = \text{veg}, \text{bare}$ [m].
$z^y_{0\text{c}}$	Scalar roughness length for surface type $y = \text{veg}, \text{bare}$ [m].
z_{ref}	Atmospheric forcing or reference height [m].
l_m	Within-canopy mixing length scale [m].
$\Psi^{\text{H\&F}}_m, \Psi^{\text{H\&F}}_c$	Harman–Finnigan RSL-corrected stability functions for momentum and scalars [−].
ψ_m, ψ_c	Monin–Obukhov stability functions for momentum and scalars [−].
$\widehat{\psi}_m, \widehat{\psi}_c$	Roughness-sublayer integral functions for momentum and scalars [−].
vkc	von Karman constant [−].
β	Ratio of friction velocity to wind speed at canopy height [−].
$u^y(z)$	Wind speed at height z over surface type $y = \text{veg}, \text{bare}$ [m s^{-1}].
u^y_*	Friction velocity for surface type $y = \text{veg}, \text{bare}$ [m s^{-1}].
$g^y_{\text{a}}(z_i, z_{i+1})$	Aerodynamic conductance between adjacent layers over surface type $y = \text{veg}, \text{bare}$ [mol m^{-2} s^{-1}].
$g^y_{\text{a,ground}}$	Aerodynamic conductance between the ground and the first model layer [mol m^{-2} s^{-1}].
ρ	Molar density of moist air [mol m^{-3}].
Sc	Turbulent Schmidt number [−].

https://doi.org/10.5194/egusphere-2026-4875
Preprint. Discussion started: 21 September 2026

Table C4. Generalized symbols for the canopy implicit solution and surface energy balance. Units are given in brackets.

Symbol	Description
$\theta_{y,i}$	Air temperature in layer i over surface type $y = \mathrm{veg}, \mathrm{bare}$ [K].
$\mathrm{qv}_{y,i}$	Specific humidity in layer i over surface type $y = \mathrm{veg}, \mathrm{bare}$ [$\mathrm{mol\,mol^{-1}}$].
$\mathrm{qv}_{\mathrm{sat}}(T)$	Saturation specific humidity at temperature T [$\mathrm{mol\,mol^{-1}}$].
$T_{\mathrm{l},x,i}$	Leaf temperature for foliage class $x = \mathrm{sun}, \mathrm{sha}$ in layer i [K].
Δz_i	Thickness of canopy layer i [m].
Δt	Model or solver time step [s].
c_p	Moist-air specific heat at constant pressure [$\mathrm{J\,mol^{-1}\,K^{-1}}$].
c_l	Leaf heat capacity per unit leaf area [$\mathrm{J\,m^{-2}\,K^{-1}}$].
λ	Latent heat of vaporization [$\mathrm{J\,mol^{-1}}$].
g_i^{bh}	Leaf boundary-layer conductance for heat [$\mathrm{mol\,m^{-2}\,s^{-1}}$].
g_i^{bv}	Leaf boundary-layer conductance for water vapor [$\mathrm{mol\,m^{-2}\,s^{-1}}$].
$g_i^{\mathrm{tot},x}$	Total conductance to transpiration for foliage class $x = \mathrm{sun}, \mathrm{sha}$ [$\mathrm{mol\,m^{-2}\,s^{-1}}$].
$g_i^{\mathrm{l},x}$	Effective leaf conductance for water vapor for foliage class $x = \mathrm{sun}, \mathrm{sha}$ [$\mathrm{mol\,m^{-2}\,s^{-1}}$].
$f_{\mathrm{wet}}^i, f_{\mathrm{dry}}^i$	Wet and dry foliage fractions in canopy layer i [$-$].
θ_{ref}	Atmospheric forcing temperature at the reference height [K].
$\mathrm{qv}_{\mathrm{ref}}$	Atmospheric forcing specific humidity at the reference height [$\mathrm{mol\,mol^{-1}}$].
$T_{y,\mathrm{ground}}$	Ground surface temperature for surface type $y = \mathrm{veg}, \mathrm{bare}$ [K].
G_y	Ground heat flux for surface type $y = \mathrm{veg}, \mathrm{bare}$ [$\mathrm{W\,m^{-2}}$].
$g_{\mathrm{tot,ground}}^y$	Total conductance for soil evaporation [$\mathrm{mol\,m^{-2}\,s^{-1}}$].
g_{soil}^y	Soil surface conductance for water vapor [$\mathrm{mol\,m^{-2}\,s^{-1}}$].
$\mathrm{rh}_{\mathrm{ground}}^y$	Relative humidity at the ground surface [$-$].
Ψ_{sfc}	Soil matric potential at the surface [m].
grav	Gravitational acceleration [$\mathrm{m\,s^{-2}}$].

https://doi.org/10.5194/egusphere-2026-4875
Preprint. Discussion started: 21 September 2026

Table C5. Generalized symbols for subsurface thermal and hydrological processes. Units are given in brackets.

Symbol	Description
N_s	Number of soil layers [$-$].
$\Delta z_{\mathrm{s},i}$	Thickness of soil layer i [m].
$Z_{\mathrm{s,max}}$	Total soil-column depth [m].
r_s	Common ratio of the geometrically stretched soil grid [$-$].
κ	Soil thermal conductivity [$\mathrm{W\,m^{-1}\,K^{-1}}$].
$\kappa_{\mathrm{sat}}, \kappa_{\mathrm{dry}}$	Saturated and dry soil thermal conductivities [$\mathrm{W\,m^{-1}\,K^{-1}}$].
K_e	Kersten number [$-$].
C_s	Volumetric soil heat capacity [$\mathrm{J\,m^{-3}\,K^{-1}}$].
$C_{\mathrm{liq/ice/soil/a}}$	Volumetric heat capacity of liquid water, ice, soil solids, or air [$\mathrm{J\,m^{-3}\,K^{-1}}$].
$\theta_{\mathrm{liq/ice/tot/sat}}$	Volumetric soil-water content for the liquid, ice, total, or saturated state [$\mathrm{m^3\,m^{-3}}$].
ψ_i	Soil matric potential in layer i [cm].
$\psi_{\mathrm{sat},i}, \psi_{\mathrm{wilt},i}$	Saturated and wilting-point matric potentials in layer i [cm].
S_e	Effective soil saturation [$-$].
α_{VG}	van Genuchten inverse air-entry potential [$\mathrm{cm^{-1}}$].
$m_{\mathrm{VG}}, n_{\mathrm{VG}}$	van Genuchten shape parameters [$-$].
$\theta_{\mathrm{r,VG}}, \theta_{\mathrm{s,VG}}$	Residual and saturated volumetric soil-water contents [$\mathrm{m^3\,m^{-3}}$].
K_{VG}	Unsaturated hydraulic conductivity from the van Genuchten formulation [$\mathrm{cm\,s^{-1}}$].
$K_{\mathrm{VG,sat}}$	Saturated hydraulic conductivity [$\mathrm{cm\,s^{-1}}$].
C_i	Specific soil-moisture capacity, $\partial\theta_{\mathrm{liq},i}/\partial\psi_i$ [$\mathrm{cm^{-1}}$].
z_s	Soil depth, positive downward [cm].
$F(z_\mathrm{s})$	Cumulative root fraction above soil depth z_s [$-$].
β_s	Jackson root-distribution parameter [$-$].
W_i	Soil-wetness factor in layer i [$-$].
R_i	Root fraction in soil layer i [$-$].
N_{root}	Number of soil layers containing roots [$-$].
$Z_{\mathrm{s},i}$	Soil or rooting depth associated with layer i [m].
$S_\mathrm{s}(z)$	Volumetric sink from soil evaporation and root-water uptake [$\mathrm{s^{-1}}$].
$S_{\mathrm{s,trans},i}$	Transpiration component of the soil-water sink in layer i [$\mathrm{s^{-1}}$].
ω	Picard-iteration damping factor [$-$].
$\Delta\psi_i$	Iterative matric-potential increment in soil layer i [cm].
$T_{\mathrm{soil},i}$	Temperature of soil layer i [K].

https://doi.org/10.5194/egusphere-2026-4875
Preprint. Discussion started: 21 September 2026

Author contributions. H.G.K. conceptualized, developed the model and software, conducted the experiments, compiled the verification datasets, validated the model and wrote the first draft of the manuscript. G.B.B. developed the CLM-ml v0 from which some parameterizations were adopted to Noah-MP-ML^2 as discussed in section 5. C.H. supervised this study and provided support with the community Noah-MP model. Z-L.Y. and D.N. were research co-advisors to H.G.K. and also supervised this study. R.A-R. developed the roughness sub-layer scheme with the community Noah-MP and helped prepare the verification and forcing datasets. A.M. provided insights on model performance and helped interpret the results, especially at the US-UMB station. All authors reviewed and approved the manuscript

Competing interests. Cenlin He is a member of the editorial board of Geoscientific Model Development (GMD). The authors have no other competing interests to declare.

Acknowledgements. C.H. was partially supported by NOAA's WPO S2S grants NA22OAR4590503 and NA25OARX459C0340. D.N. acknowledges support from National Aeronautics and Space Administration (NASA) IDS grant 80NSSC20K1262 and U.S. Department of Energy (DoE) Urban Integrated Field Lab Community Research on Climate and Urban Science (CROCUS) grant number DE-SC0023226. NCAR is sponsored by the National Science Foundation (NSF). Any opinions, findings, conclusions, or recommendations expressed in this publication are those of the authors and do not necessarily reflect the views of NSF.

https://doi.org/10.5194/egusphere-2026-4875
Preprint. Discussion started: 21 September 2026

References

Abolafia-Rosenzweig, R., He, C., Burns, S. P., and Chen, F.: Implementation and Evaluation of a Unified Turbulence Parameterization Throughout the Canopy and Roughness Sublayer in Noah-MP Snow Simulations, Journal of Advances in Modeling Earth Systems, 13, e2021MS002 665, https://doi.org/10.1029/2021MS002665, 2021.

Baldocchi, D. D. and Harley, P. C.: Scaling carbon dioxide and water vapour exchange from leaf to canopy in a deciduous forest. II. Model testing and application, Plant, Cell & Environment, 18, 1157–1173, https://doi.org/10.1111/j.1365-3040.1995.tb00626.x, 1995.

Ball, J. T., Woodrow, I. E., and Berry, J. A.: A Model Predicting Stomatal Conductance and its Contribution to the Control of Photosynthesis under Different Environmental Conditions, in: Progress in Photosynthesis Research, edited by Biggins, J., pp. 221–224, Springer Netherlands, Dordrecht, https://doi.org/10.1007/978-94-017-0519-6_48, 1987.

Bonan, G. B., Williams, M., Fisher, R. A., and Oleson, K. W.: Modeling stomatal conductance in the earth system: linking leaf water-use efficiency and water transport along the soil–plant–atmosphere continuum, Geoscientific Model Development, 7, 2193–2222, https://doi.org/10.5194/gmd-7-2193-2014, 2014.

Bonan, G. B., Patton, E. G., Harman, I. N., Oleson, K. W., Finnigan, J. J., Lu, Y., and Burakowski, E. A.: Modeling canopy-induced turbulence in the Earth system: a unified parameterization of turbulent exchange within plant canopies and the roughness sublayer (CLM-ml v0), Geoscientific Model Development, 11, 1467–1496, https://doi.org/10.5194/gmd-11-1467-2018, 2018.

Campbell, G. S.: A simple method for determining unsaturated conductivity from moisture retention data, Soil Science, 117, 311–314, https://doi.org/10.1097/00010694-197406000-00001, 1974.

Carsel, R. F. and Parrish, R. S.: Developing joint probability distributions of soil water retention characteristics, Water Resources Research, 24, 755–769, https://doi.org/10.1029/WR024i005p00755, 1988.

Celia, M. A., Bouloutas, E. T., and Zarba, R. L.: A general mass-conservative numerical solution for the unsaturated flow equation, Water Resources Research, 26, 1483–1496, https://doi.org/10.1029/WR026i007p01483, 1990.

Chavoshi, A., Dashtian, H., Bakhshian, S., Young, M. H., and Niyogi, D.: PINN-SM: A Physics-Informed Neural Networks Model for Vadose Zone Soil Moisture Profile Prediction, Journal of Geophysical Research: Machine Learning and Computation, 2, e2024JH000 547, https://doi.org/10.1029/2024JH000547, 2025.

Chen, F. and Dudhia, J.: Coupling an Advanced Land Surface–Hydrology Model with the Penn State–NCAR MM5 Modeling System. Part I: Model Implementation and Sensitivity, Monthly Weather Review, 129, 569–585, https://doi.org/10.1175/1520-0493(2001)129<0569:CAALSH>2.0.CO;2, 2001.

Chen, F., Manning, K. W., LeMone, M. A., Trier, S. B., Alfieri, J. G., Roberts, R., Tewari, M., Niyogi, D., Horst, T. W., Oncley, S. P., Basara, J. B., and Blanken, P. D.: Description and Evaluation of the Characteristics of the NCAR High-Resolution Land Data Assimilation System, Journal of Applied Meteorology and Climatology, 46, 694–713, https://doi.org/10.1175/JAM2463.1, 2007.

Clapp, R. B. and Hornberger, G. M.: Empirical equations for some soil hydraulic properties, Water Resources Research, 14, 601–604, https://doi.org/10.1029/WR014i004p00601, 1978.

Deardorff, J. W.: Efficient prediction of ground surface temperature and moisture, with inclusion of a layer of vegetation, Journal of Geophysical Research: Oceans, 83, 1889–1903, https://doi.org/10.1029/JC083iC04p01889, 1978.

Dickinson, R. E.: Land Surface Processes and Climate—Surface Albedos and Energy Balance, in: Theory of Climate, vol. 25 of *Advances in Geophysics*, pp. 305–353, Elsevier, https://doi.org/10.1016/S0065-2687(08)60176-4, 1983.

https://doi.org/10.5194/egusphere-2026-4875
Preprint. Discussion started: 21 September 2026

Dickinson, R. E., Henderson-Sellers, A., Kennedy, P. J., and Wilson, M. F.: Biosphere–Atmosphere Transfer Scheme (BATS) for the NCAR Community Climate Model, NCAR Technical Note NCAR/TN-275+STR, National Center for Atmospheric Research, Boulder, Colorado, https://doi.org/10.5065/D6668B58, 1986.

Ek, M. B., Mitchell, K. E., Lin, Y., Rogers, E., Grunmann, P., Koren, V., Gayno, G., and Tarpley, J. D.: Implementation of Noah land surface model advances in the National Centers for Environmental Prediction operational mesoscale Eta model, Journal of Geophysical Research: Atmospheres, 108, 8851, https://doi.org/10.1029/2002JD003296, 2003.

Farquhar, G. D., von Caemmerer, S., and Berry, J. A.: A Biochemical Model of Photosynthetic CO_2 Assimilation in Leaves of C_3 Species, Planta, 149, 78–90, https://doi.org/10.1007/BF00386231, 1980.

Franks, P. J., Berry, J. A., Lombardozzi, D. L., and Bonan, G. B.: Stomatal Function across Temporal and Spatial Scales: Deep-Time Trends, Land–Atmosphere Coupling and Global Models, Plant Physiology, 174, 583–602, https://doi.org/10.1104/pp.17.00287, 2017.

Frasson, R. P. d. M., Bohrer, G., Medvigy, D., Matheny, A. M., Morin, T. H., Vogel, C. S., Gough, C. M., Maurer, K. D., and Curtis, P. S.: Modeling Forest Carbon Cycle Response to Tree Mortality: Effects of Plant Functional Type and Disturbance Intensity, Journal of Geophysical Research: Biogeosciences, 120, 2178–2193, https://doi.org/10.1002/2015JG003035, 2015.

Garratt, J. R.: Surface influence upon vertical profiles in the atmospheric near-surface layer, Quarterly Journal of the Royal Meteorological Society, 106, 803–819, https://doi.org/10.1002/qj.49710645011, 1980.

Goudriaan, J.: Crop Micrometeorology: A Simulation Study, Simulation Monographs, Centre for Agricultural Publishing and Documentation (Pudoc), Wageningen, ISBN 978-90-220-0614-6, 1977.

Gough, C., Bohrer, G., and Curtis, P.: FLUXNET2015 US-UMB Univ. of Mich. Biological Station, https://doi.org/10.18140/FLX/1440093, dataset, 2015.

Gupta, H. V., Kling, H., Yilmaz, K. K., and Martinez, G. F.: Decomposition of the mean squared error and NSE performance criteria: Implications for improving hydrological modelling, Journal of Hydrology, 377, 80–91, https://doi.org/10.1016/j.jhydrol.2009.08.003, 2009.

Harman, I. N. and Finnigan, J. J.: A Simple Unified Theory for Flow in the Canopy and Roughness Sublayer, Boundary-Layer Meteorology, 123, 339–363, https://doi.org/10.1007/s10546-006-9145-6, 2007.

Harman, I. N. and Finnigan, J. J.: Scalar Concentration Profiles in the Canopy and Roughness Sublayer, Boundary-Layer Meteorology, 129, 323–351, https://doi.org/10.1007/s10546-008-9328-4, 2008.

Haverkamp, R., Vauclin, M., Touma, J., Wierenga, P. J., and Vachaud, G.: A Comparison of Numerical Simulation Models for One-Dimensional Infiltration, Soil Science Society of America Journal, 41, 285–294, https://doi.org/10.2136/sssaj1977.03615995004100020024x, 1977.

He, C., Barlage, M., Valayamkunnath, P., Gill, D., Mocko, D., and Chen, F.: NCAR/noahmp: Release of v5.0.0, https://doi.org/10.5281/zenodo.7901854, software, 2023a.

He, C., Valayamkunnath, P., Barlage, M., Chen, F., Gochis, D., Cabell, R., Schneider, T., Rasmussen, R., Niu, G.-Y., Yang, Z.-L., Niyogi, D., and Ek, M.: Modernizing the open-source community Noah with multi-parameterization options (Noah-MP) land surface model (version 5.0) with enhanced modularity, interoperability, and applicability, Geoscientific Model Development, 16, 5131–5151, https://doi.org/10.5194/gmd-16-5131-2023, 2023b.

He, C., Valayamkunnath, P., Barlage, M., Chen, F., Gochis, D., Cabell, R., Schneider, T., Rasmussen, R., Niu, G.-Y., Yang, Z.-L., Niyogi, D., and Ek, M.: The Community Noah-MP Land Surface Modeling System Technical Description Version 5.0, Tech. rep., NSF National Center for Atmospheric Research, Boulder, Colorado, https://doi.org/10.5065/EW8G-YR95, 2023c.

https://doi.org/10.5194/egusphere-2026-4875
Preprint. Discussion started: 21 September 2026

Hogan, R. J.: Flexible Treatment of Radiative Transfer in Complex Urban Canopies for Use in Weather and Climate Models, Boundary-Layer Meteorology, 173, 53–78, https://doi.org/10.1007/s10546-019-00457-0, 2019.

Hogan, R. J., Quaife, T., and Braghiere, R.: Fast matrix treatment of 3-D radiative transfer in vegetation canopies: SPARTACUS-Vegetation 1.1, Geoscientific Model Development, 11, 339–350, https://doi.org/10.5194/gmd-11-339-2018, 2018.

Jackson, R. B., Canadell, J., Ehleringer, J. R., Mooney, H. A., Sala, O. E., and Schulze, E.-D.: A global analysis of root distributions for terrestrial biomes, Oecologia, 108, 389–411, https://doi.org/10.1007/BF00333714, 1996.

Jarvis, P. G.: The interpretation of the variations in leaf water potential and stomatal conductance found in canopies in the field, Philosophical Transactions of the Royal Society of London. B, Biological Sciences, 273, 593–610, https://doi.org/10.1098/rstb.1976.0035, 1976.

Kaimal, J. C. and Finnigan, J. J.: Atmospheric Boundary Layer Flows: Their Structure and Measurement, Oxford University Press, New York, ISBN 978-0-19-506239-7, https://doi.org/10.1093/oso/9780195062397.001.0001, 1994.

Kamath, H., Bonan, G., Yang, Z.-L., Abolafia-Rosenzweig, R., He, C., Matheny, A. M., and Niyogi, D.: Noah-MP-ML^2: Multilayer canopy land surface model with improved representation of vadose zone soil water dynamics, https://doi.org/10.5281/zenodo.21908465, 2026.

Kavetski, D., Binning, P., and Sloan, S. W.: Adaptive time stepping and error control in a mass conservative numerical solution of the mixed form of Richards equation, Advances in Water Resources, 24, 595–605, https://doi.org/10.1016/S0309-1708(00)00076-2, 2001.

Knohl, A., Tiedemann, F., Kolle, O., Schulze, E.-D., Kutsch, W., Herbst, M., and Siebicke, L.: FLUXNET2015 DE-Hai Hainich, https://doi.org/10.18140/FLX/1440148, dataset, 2016.

Law, B.: FLUXNET2015 US-Me2 Metolius mature ponderosa pine, https://doi.org/10.18140/FLX/1440079, dataset, 2016.

Li, L., Yang, Z.-L., Matheny, A. M., Zheng, H., Swenson, S. C., Lawrence, D. M., Barlage, M., Yan, B., McDowell, N. G., and Leung, L. R.: Representation of Plant Hydraulics in the Noah-MP Land Surface Model: Model Development and Multiscale Evaluation, Journal of Advances in Modeling Earth Systems, 13, e2020MS002 214, https://doi.org/10.1029/2020MS002214, 2021.

Lin, T.-S., He, C., Liu, C., Abolafia-Rosenzweig, R., Dudhia, J., Barlage, M. J., Zhang, Z., and Newman, A. J.: Soil Organic Matter Reduces Persistent Nighttime Surface Warm Bias in Convection-Permitting U.S. Simulations, Geophysical Research Letters, 53, e2026GL123 274, https://doi.org/10.1029/2026GL123274, 2026.

Manabe, S.: Climate and the Ocean Circulation: I. The Atmospheric Circulation and the Hydrology of the Earth's Surface, Monthly Weather Review, 97, 739–774, https://doi.org/10.1175/1520-0493(1969)097<0739:CATOC>2.3.CO;2, 1969.

Matheny, A. M., Bohrer, G., Vogel, C. S., Morin, T. H., He, L., Frasson, R. P. d. M., Mirfenderesgi, G., Schäfer, K. V. R., Gough, C. M., Ivanov, V. Y., and Curtis, P. S.: Species-Specific Transpiration Responses to Intermediate Disturbance in a Northern Hardwood Forest, Journal of Geophysical Research: Biogeosciences, 119, 2292–2311, https://doi.org/10.1002/2014JG002804, 2014.

Medlyn, B. E., Duursma, R. A., Eamus, D., Ellsworth, D. S., Prentice, I. C., Barton, C. V. M., Crous, K. Y., De Angelis, P., Freeman, M., and Wingate, L.: Reconciling the optimal and empirical approaches to modelling stomatal conductance, Global Change Biology, 17, 2134–2144, https://doi.org/10.1111/j.1365-2486.2010.02375.x, 2011.

Monteith, J. L. and Unsworth, M. H.: Principles of Environmental Physics: Plants, Animals, and the Atmosphere, Academic Press, 4 edn., ISBN 978-0-12-386910-4, https://www.sciencedirect.com/book/9780123869104/principles-of-environmental-physics, 2013.

Niu, G.-Y. and Yang, Z.-L.: Effects of vegetation canopy processes on snow surface energy and mass balances, Journal of Geophysical Research: Atmospheres, 109, D23 111, https://doi.org/10.1029/2004JD004884, 2004.

Niu, G.-Y., Yang, Z.-L., Mitchell, K. E., Chen, F., Ek, M. B., Barlage, M., Kumar, A., Manning, K., Niyogi, D., Rosero, E., Tewari, M., and Xia, Y.: The community Noah land surface model with multiparameterization options (Noah-MP): 1. Model description and evaluation

https://doi.org/10.5194/egusphere-2026-4875
Preprint. Discussion started: 21 September 2026

with local-scale measurements, Journal of Geophysical Research: Atmospheres, 116, D12 109, https://doi.org/10.1029/2010JD015139, 2011.

Norman, J. M.: Modeling the Complete Crop Canopy, in: Modification of the Aerial Environment of Plants, edited by Barfield, B. J. and Gerber, J. F., no. 2 in ASAE Monograph, pp. 249–280, American Society of Agricultural Engineers, St. Joseph, Michigan, 1979.

Novick, K. and Phillips, R.: FLUXNET2015 US-MMS Morgan Monroe State Forest, https://doi.org/10.18140/FLX/1440083, dataset, 2016.

Paniconi, C. and Putti, M.: A comparison of Picard and Newton iteration in the numerical solution of multidimensional variably saturated flow problems, Water Resources Research, 30, 3357–3374, https://doi.org/10.1029/94WR02046, 1994.

Peters-Lidard, C. D., Blackburn, E., Liang, X., and Wood, E. F.: The Effect of Soil Thermal Conductivity Parameterization on Surface Energy Fluxes and Temperatures, Journal of the Atmospheric Sciences, 55, 1209–1224, https://doi.org/10.1175/1520-0469(1998)055<1209:TEOSTC>2.0.CO;2, 1998.

Pitman, A. J.: The evolution of, and revolution in, land surface schemes designed for climate models, International Journal of Climatology, 23, 479–510, https://doi.org/10.1002/joc.893, 2003.

Raupach, M. R. and Thom, A. S.: Turbulence in and above Plant Canopies, Annual Review of Fluid Mechanics, 13, 97–129, https://doi.org/10.1146/annurev.fl.13.010181.000525, 1981.

Richards, L. A.: Capillary Conduction of Liquids through Porous Mediums, Physics, 1, 318–333, https://doi.org/10.1063/1.1745010, 1931.

Ross, J.: Radiative Transfer in Plant Communities, in: Vegetation and the Atmosphere, Volume 1: Principles, edited by Monteith, J. L., pp. 13–55, Academic Press, London and New York, 1975.

Ross, J.: The Radiation Regime and Architecture of Plant Stands, vol. 3 of *Tasks for Vegetation Science*, Dr W. Junk Publishers, The Hague, ISBN 978-90-6193-607-7, https://doi.org/10.1007/978-94-009-8647-3, 1981.

Ryder, J., Polcher, J., Peylin, P., Ottlé, C., Chen, Y.-P., van Gorsel, E., Haverd, V., McGrath, M. J., Naudts, K., Otto, J., Valade, A., and Luyssaert, S.: A multi-layer land surface energy budget model for implicit coupling with global atmospheric simulations, Geoscientific Model Development, 9, 223–245, https://doi.org/10.5194/gmd-9-223-2016, 2016.

Sakaguchi, K. and Zeng, X.: Effects of soil wetness, plant litter, and under-canopy atmospheric stability on ground evaporation in the Community Land Model (CLM3.5), Journal of Geophysical Research: Atmospheres, 114, D01 107, https://doi.org/10.1029/2008JD010834, 2009.

Schaake, J. C., Koren, V. I., Duan, Q.-Y., Mitchell, K., and Chen, F.: Simple water balance model for estimating runoff at different spatial and temporal scales, Journal of Geophysical Research: Atmospheres, 101, 7461–7475, https://doi.org/10.1029/95JD02892, 1996.

Sellers, P. J.: Canopy reflectance, photosynthesis and transpiration, International Journal of Remote Sensing, 6, 1335–1372, https://doi.org/10.1080/01431168508948283, 1985.

Sellers, P. J., Mintz, Y., Sud, Y. C., and Dalcher, A.: A Simple Biosphere Model (SiB) for Use within General Circulation Models, Journal of the Atmospheric Sciences, 43, 505–531, https://doi.org/10.1175/1520-0469(1986)043<0505:ASBMFU>2.0.CO;2, 1986.

Taylor, K. E.: Summarizing multiple aspects of model performance in a single diagram, Journal of Geophysical Research: Atmospheres, 106, 7183–7192, https://doi.org/10.1029/2000JD900719, 2001.

van Genuchten, M. T.: A Closed-form Equation for Predicting the Hydraulic Conductivity of Unsaturated Soils, Soil Science Society of America Journal, 44, 892–898, https://doi.org/10.2136/sssaj1980.03615995004400050002x, 1980.

Waggoner, P. E. and Reifsnyder, W. E.: Simulation of the Temperature, Humidity and Evaporation Profiles in a Leaf Canopy, Journal of Applied Meteorology, 7, 400–409, https://doi.org/10.1175/1520-0450(1968)007<0400:SOTTHA>2.0.CO;2, 1968.

https://doi.org/10.5194/egusphere-2026-4875
Preprint. Discussion started: 21 September 2026

Widlowski, J.-L., Pinty, B., Clerici, M., Dai, Y., De Kauwe, M., De Ridder, K., Kallel, A., Kobayashi, H., Lavergne, T., Ni-Meister, W., Olchev, A., Quaife, T., Wang, S., Yang, W., Yang, Y., and Yuan, H.: RAMI4PILPS: An intercomparison of formulations for the partitioning of solar radiation in land surface models, Journal of Geophysical Research: Biogeosciences, 116, G02 019, https://doi.org/10.1029/2010JG001511, 2011.

Woodgate, W., van Gorsel, E., and Leuning, R.: FLUXNET2015 AU-Tum Tumbarumba, https://doi.org/10.18140/FLX/1440126, dataset, 2016.

Yang, Z.-L., Niu, G.-Y., Mitchell, K. E., Chen, F., Ek, M. B., Barlage, M., Longuevergne, L., Manning, K., Niyogi, D., Tewari, M., and Xia, Y.: The community Noah land surface model with multiparameterization options (Noah-MP): 2. Evaluation over global river basins, Journal of Geophysical Research: Atmospheres, 116, D12 110, https://doi.org/10.1029/2010JD015140, 2011.